

Supplementary Information for

Taming Hurricanes With Arrays of Offshore Wind Turbines

Mark Z. Jacobson, Cristina L. Archer, Willett Kempton
Nature Climate Change

Received September 23, 2013

Accepted January 3, 2014

This PDF file includes:

- S1. Supporting Materials and Methods
- S2. Supporting Cost Analysis
- S3. Supporting Figures
- S4. Supporting References and Notes

S1. Supporting Materials and Methods

For this study, the GATOR-GCMOM (Gas, Aerosol, Transport, Radiation, General Circulation, Mesoscale, and Ocean Model) global-through-local climate-pollution-weather-forecast model (S1-S3) was used to simulate the effect of installing large arrays of wind turbines on hurricane dissipation. The model was run without data assimilation. This was necessary for examining the effects of wind turbine energy extraction on hurricane dissipation. The reason is that many pairs of simulations, one with turbines and the other without turbines, were run. If data were assimilated in simulations with and without turbines, feedbacks from wind turbines would be overridden by observed meteorology and could not naturally occur in the model. As such, the impact of turbine energy extraction on clouds, for example, could not be simulated correctly. In sum, an operational hurricane model that assimilates data cannot be used for this application.

GATOR-GCMOM allows either stretched or nested (from the global to local scales) domains. It simulates feedbacks among meteorology, radiation, gases, aerosol particles, cloud hydrometeor particles, oceans, sea ice, snow, soil, vegetation, and radiation. The model extracts the correct amount of energy from the wind at different model heights intersecting each turbine rotor blade based on the turbine power curve, as described in Section S1.H and in (S1). It also accounts for feedback of wind speed changes to energy and moisture fluxes at the surface, as do other models of

wind turbine impacts, including limited-area domain high-resolution models (S4, S5). Below, the model is briefly described.

S1.A. Atmospheric Meteorology and Transport

The momentum, thermodynamic energy, and continuity equations were solved for the atmosphere with a potential-ensrophy, vorticity, energy, and mass-conserving scheme (S6). Winds and turbulence predicted by the model drove the horizontal and vertical transport of gases and size- and composition-resolved aerosol particles, solved with a monotonic advection scheme (S7). Subgrid turbulent kinetic energy was calculated as a function of instantaneous modeled grid-scale wind shear and buoyancy as well as shear due to wind turbines themselves (Section S1.H.)

S1.B. Subgrid Ocean, Sea Ice, Land, Vegetation, and Snow Surfaces

The model treated 17 subgrid surface classes in each grid cell and energy and vapor exchange between the atmosphere and each subgrid surface in each cell. The surface classes included 13 soil classes, water bodies, roads, roofs, and deep snow/ice. Sea ice could form on top of water, and snow could deposit on sea ice and land (S2, S8). Within each land grid cell, soil temperatures and moisture were calculated over time separately for each subgrid soil class in each of 10 subsurface soil layers with top-to-bottom layer thicknesses of 0.005, 0.01, 0.01, 0.01, 0.015, 0.025, 0.05, 0.1, 5, and 5 m, respectively. Thus, subgrid, subsurface temperatures and moisture were tracked perpetually and independently throughout each simulation. The same 10-layer subsurface module was applied to permanent snow (e.g., over the Antarctic) and to roads and roofs.

On land surfaces, each subgrid soil class was divided into vegetated and bare soil. Snow could accumulate on soil and vegetation. For bare and vegetated soil, the surface energy balance equation accounted for latent heat, sensible heat, solar, thermal-IR, and conductive energy fluxes. However, for vegetated soil, the fluxes took into account the foliage temperature and moisture as well as the temperature and moisture of the air within the foliage, all of which were tracked prognostically in time or diagnostically from prognostic parameters by iteration (S2). Foliage temperature and moisture were a function of evapotranspiration, which conserved water in the model. When snow was on top of vegetation or bare soil (not so relevant for the present simulations, except at high latitudes), an additional model layer with thickness equal to that of the snow was added to the 10-layer subsurface module.

Oceans in the model were represented in 3-D for some calculations and 2-D for others. A 2-D time-dependent mixed-layer ocean dynamics model driven by surface wind stress was used to solve for mixed-layer velocities, heights, and horizontal energy transport in each grid cell (S9). The scheme conserved potential enstrophy, vorticity, energy, and mass and predicted gyres and major currents. Energy diffusion to the deep ocean was treated in 3-D through 10 ocean layers below each surface ocean grid cell. Air-ocean exchange, vertical diffusion through the ocean, and 3-D ocean equilibrium chemistry and pH were solved among the Na-Cl-Mg-Ca-K-H-O-Li-Sr-C-S-N-Br-F-B-Si-P system as in (S10). Drag at the ocean surface, a parameter

important for hurricane intensification, was calculated as a function of 10-m wind speed that increased well into the hurricane wind speed range (*S11*). Sea ice in the model (relevant here only at high latitudes) formed, evolved, and flowed horizontally on subgrid water surfaces, and snow could accumulate on sea ice.

S1.C. Gas Processes

Gas processes included emissions, gas photochemistry, gas-to-particle conversion, gas-to-cloud conversion, gas-cloud exchange, gas-precipitation exchange, gas-ocean exchange, advection, convection, molecular diffusion, turbulent diffusion, and dry deposition. Gas photochemistry was solved with SMVGEAR II (*S12*) for ~180 species and ~440 tropospheric and stratospheric kinetic, particle surface (heterogeneous), and photolysis reactions.

S1.D. Aerosol Processes

Aerosol processes included anthropogenic and natural emissions, binary and ternary homogeneous nucleation, condensation, dissolution, internal-particle chemical equilibrium, aerosol-aerosol coagulation, aerosol activation of clouds, aerosol-hydrometeor coagulation, sedimentation, dry deposition, and transport (*S13*, *S14*). Chemical equilibrium calculations included the determination of the solid/liquid/ion composition, pH, and liquid water content of aerosols as a function of size. The model can treat any number of discrete aerosol size distributions, each with any number of discrete size bins and chemicals per size bin. Particle number and chemical mole concentrations are tracked in each grid cell. The components within each size bin of each aerosol size distribution are internally mixed in the bin but externally mixed from other bins and other size distributions.

S1.E. Clouds and Aerosol-Cloud Processes

Aerosol-cloud interactions and cloud/precipitation evolution in GATOR-GCMOM were treated as explicitly as possible. The model simulated the size- and composition-resolved microphysical evolution of clouds and precipitation, the first and second aerosol indirect effects, the semi-direct effect, and cloud absorption effects (which are the heating of a cloud due to solar absorption by absorbing inclusions in cloud drops and swollen absorbing aerosol particles interstitially between cloud drops). Microphysical processes were treated with discrete, size- and composition resolution for both aerosol particles and hydrometeor particles, as described in Figure S1 and (*S14*, *S15*).

During nesting, both cloud thermodynamics and microphysics were solved explicitly at the grid scale in the finest domains (*S13*). For global-through-local stretched domains, the cloud treatment must be consistent over all grid cell sizes, so although cloud microphysics was solved explicitly with size and composition resolution, cloud thermodynamics was parameterized to treat multiple subgrid cumulus clouds in each column based on an Arakawa-Schubert treatment as described in (*S16*). In that case, all aerosols and gases were convected vertically within each subgrid cloud (up to 500 convective clouds per grid cell, each with a different base and top, but often just one in high-resolution grid cells). However, all cloud and precipitation microphysical

processes were time-dependent, explicit, and size- and composition-resolved. Explicit, grid-scale thermodynamics was not used for the stretched domain because such a treatment results in coarse grid cells being covered entirely with water and with very small vertical velocities. However, the stretched grid approach can be preferable to the nested grid approach for hurricanes since the stretched grid approach does not suffer from uncertainties induced at domain boundaries. On the other hand, the nested approach allows for finer resolution in the region of interest for a given computer time.

One additional feature of the cloud treatment relevant to hurricanes is that water vapor was a component of air pressure in the model; thus, reductions in water vapor due to its conversion to cloud water followed by precipitation helped contribute to the drop in air pressure in the hurricane.

S1.F. Aerosol and Hydrometeor Size Distribution, Composition, and Interactions

Three discrete (multiple size bin) aerosol size distributions and three discrete hydrometeor distributions were used. The three aerosol distributions were an emitted fossil-fuel soot (EFFS) distribution, an emitted combined biofuel-soot and biomass-burning-soot (BFBB) distribution, and an internally-mixed (IM) distribution. Each size distribution contained 14 size bins. The three hydrometeor distributions were liquid, ice, and graupel distributions (Figure S1), each with 30 size bins (0.5 μm to 8 mm in diameter). Each size bin of the EFFS aerosol distribution contained black carbon (BC), weakly-to-moderately-absorbing primary organic matter (POM), secondary organic matter (SOM), hydrated liquid water, $\text{H}_2\text{SO}_4(\text{aq})$, HSO_4^- , SO_4^{2-} , NO_3^- , Cl^- , H^+ , NH_4^+ , $\text{NH}_4\text{NO}_3(\text{s})$, and $(\text{NH}_4)_2\text{SO}_4(\text{s})$. Each size bin of the BFBB distribution contained these same components plus tar balls (a strongly-absorbing form of brown carbon), Na^+ , K^+ , Ca^{2+} , and Mg^{2+} . Each size bin of the IM distribution contained the same components as the EFFS and BFBB distributions plus soil dust, pollen, spores, and bacteria. Each size bin of each hydrometeor distribution contains the same components as in all three aerosol distributions plus condensed liquid water or deposited ice.

Gases, such as HNO_3 , HCl , NH_3 , H_2SO_4 , and organics condensed onto or dissolved into EFFS, BFBB, and IM particles and dissolved within liquid hydrometeor particles or reacted on ice and graupel particle surfaces. During coagulation, the chemical components within each original coagulating particle of each size moved with the total particle to the correct size bin of the resulting aerosol or hydrometeor size distribution. Thus, aerosol particles and their components were tracked within hydrometeor particles through cloud formation and precipitation and to snow or sea ice below. When precipitation fell to snow or sea ice, the aerosol inclusions were added to the top of the snow or ice and slowly migrated through the snow or ice. The inclusions affected radiative heating of the snow or ice layer, as described shortly.

Sea spray and spume drop particles, which are relevant to hurricane studies, were emitted as a function of size and wind speed into the IM aerosol distribution,

accounting for white-cap formation at high wind speed (*S17, S18*). The treatment also accounted for the faster deposition rate of larger spume drops by solving emissions simultaneously with sedimentation. A worldwide sea spray net emission budget is given in (*S19*).

S1.G. Radiative Processes

For radiative calculations, each model column was divided into clear- and cloudy-sky columns, and separate calculations were performed for each. Radiative transfer was solved simultaneously through multiple layers of air and one snow, sea ice, or ocean water layer at the bottom to calculate, rather than prescribe, spectral albedos over these surfaces. Since the model tracked black carbon, brown carbon, soil dust, and all other aerosol inclusions within precipitation, which fell onto snow and sea ice, the radiative transfer calculation accounted for the optics of all these absorbing aerosol constituents within and between snow and sea ice particles as well as within aerosol particles and within and between cloud and precipitation particles. The optical properties of snow and sea ice containing absorbing cores were calculated from Mie theory assuming an equivalent radius of snow or ice. The radius varied with the age of the snow as a function of temperature and temperature gradient (*S20*). In sum, the model treated both the microphysical and radiative effects of aerosols on clouds, precipitation, snow, and sea ice.

The radiative code used (*21*) solved for atmospheric heating rates and actinic fluxes over each of 694 wavelengths/probability intervals with gas absorption coefficients from (*S22*), which were parameterized for each wavelength/interval by applying the multiple-absorber correlated-k distribution spectral-mapping method to line-by-line gas absorption data. Aerosol and cloud optical properties were calculated by integrating spectral optical properties over each size bin of each aerosol and hydrometeor particle size distribution. In aerosol particles, black carbon was treated as a core surrounded by a mixed shell for optical calculations (*S23*). UV and short-visible absorption by organic carbon were accounted for, allowing for optical treatment of “brown carbon”, including tar balls (*S15, S24, S25*). Since all aerosol component concentrations were tracked in each size of each hydrometeor particle type (liquid, ice, and graupel) throughout the evolution of clouds and precipitation, the model accounted for cloud absorption due to soil dust, BC, and BrC inclusions tracked in size-resolved hydrometeor particles, including those in hurricanes. Such inclusions were relevant given the substantial presence of Saharan soil dust, in particular, in Atlantic hurricanes (*S26, S27, S28*).

For each size of a cloud liquid, ice, or graupel particle, BC, BrC, and soil dust inclusions were treated as polydisperse spherules randomly dispersed throughout cloud particles whose optical properties were calculated with the iterative dynamic effective medium approximation (DEMA) (*S29*), as described in (*S15*).

S1.H. Treatment of Wind Turbine Energy Extraction

The treatment of energy extraction by wind turbines was the same as that in (*S1*), except that (*S1*) performed simulations over single regular grid domains of either

4°x5°, 2°x2.5°, or 1.5°x1.5° horizontal resolution, whereas here, a single stretched domain from the global to local scale and a nested global-through-local nested domain were used (Section S1.I). At the finest horizontal resolutions here (0.1°x0.1° for the stretched domain and 0.06° x0.08° for the nested simulation), wind turbines were not resolved in the horizontal, but they were resolved in the vertical, with five layers per turbine; nevertheless, all turbines extracted the precise amount of energy from the wind as their power curve dictated, as discussed next.

In (S1), kinetic energy extraction by wind turbines was treated by considering extraction at the height of each turbine, similarly to as in (S30), who calculated regional scale extraction, but with differences as described in (S1). In (S1) and here, each turbine was characterized by a rated power (P_t , e.g., 5 MW or 7.58 MW), a rotor diameter (D , e.g., 126 m or 127 m), a hub height above the topographical or ocean surface (H , e.g., 100 m), and a characteristic spacing area (m^2) $A_t = xD \times yD$, usually determined by convention to minimize interference of the wake of one turbine with the next. In this equation, x and y are constants that provide distances perpendicular to and parallel to, respectively, the prevailing wind direction. Some values used previously have been $x=4, y=7$; $x=3, y=10$ (S31). The maximum number of turbines in the grid cell is $N_t = A_c / A_t$, where A_c is the ground area occupied by the cell (m^2). The installed turbine density = P / A (W/m^2). Higher density implies less spacing between turbines.

For determining extraction of energy, each turbine was assumed to intersect several atmospheric vertical layers of a grid column. The momentum extracted from each layer k that the turbine intersected was proportional to the ratio of the swept area of the turbine residing in the layer (S_k) to the total swept area (m^2) of the turbine, $S_t = \pi D^2 / 4$. The swept area residing in a layer was determined from geometry. For example, the swept area falling in the lowest layer of Figure S2 (ABCD) was the area HADCH minus the area HABCH. Since the hub height (point H) and the height above the ground of the edge of each layer (e.g., point B) were known, the vertical distance HB was also known. Since the distance HC, which is the turbine radius $R = D/2$, was also known, the angle BHC was $\theta_{BHC} = \arccos(HB/R)$. Therefore, area HADCH = $2\theta_{BHC} S_t / 2\pi$, and area HABCH = $HB \times R \sin(\theta_{BHC})$. The areas of subsequent layers were calculated from bottom to top in a similar manner, taking into account the summed areas determined already.

Kinetic energy was extracted from each model layer that intersected the turbine rotor each time step Δt due to conversion of the kinetic energy to electric power by the turbine. The model used the Arakawa C grid structure; thus, u scalar velocities were located at the west ($i-1/2, j$) and east ($i+1/2, j$) edges of each grid cell in each layer k , v scalar velocities were located at the south ($i, j-1/2$) and north ($i, j+1/2$) edges, and mass M (kg) and other scalars were located at the center (i, j, k) of the cell. As such, the initial (subscript I) total kinetic energy in grid cell i, j, k before energy extraction was

$$E_{1,i,j,k} = 0.5 \left(E_{1,i-1/2,j,k} + E_{1,i+1/2,j,k} + E_{1,i,j-1/2,k} + E_{1,i,j+1/2,k} \right) \quad (S1)$$

In this equation,

$$\begin{aligned} E_{1,i-1/2,j,k} &= 0.5 M_{i-1/2,j,k} u_{1,i-1/2,j,k}^2 \quad \text{where} \quad M_{i-1/2,j,k} = 0.5 \left(M_{i-1,j,k} + M_{i,j,k} \right) \\ E_{1,i+1/2,j,k} &= 0.5 M_{i+1/2,j,k} u_{1,i+1/2,j,k}^2, \quad \text{where} \quad M_{i+1/2,j,k} = 0.5 \left(M_{i,j,k} + M_{i+1,j,k} \right) \\ E_{1,i,j-1/2,k} &= 0.5 M_{i,j-1/2,k} v_{1,i,j-1/2,k}^2, \quad \text{where} \quad M_{i,j-1/2,k} = 0.5 \left(M_{i,j-1,k} + M_{i,j,k} \right) \\ E_{1,i,j+1/2,k} &= 0.5 M_{i,j+1/2,k} v_{1,i,j+1/2,k}^2, \quad \text{where} \quad M_{i,j+1/2,k} = 0.5 \left(M_{i,j,k} + M_{i,j+1,k} \right) \end{aligned} \quad (S2)$$

The average horizontal wind speed at the vertical and horizontal center of a cell, used to determine kinetic energy extraction by a wind turbine to produce electricity, was thus $W_{i,j,k} = [2E_{1,i,j,k}/M_{i,j,k}]^{1/2}$. Each time step, the kinetic energy extracted from the turbine in a given cell was calculated as

$$\Delta E_{i,j,k} = P_{i,j,k} \Delta t S_k / S_t \quad (S3)$$

where $P_{i,j,k}$ is the power extracted from the turbine at instantaneous wind speed $W_{i,j,k}$ based on its power curve. Equation S3 implies that the power determined from the power curve was calculated with a different wind speed in each model layer intersecting the turbine. Whereas power curves are derived based on the wind speed at hub height, the assumption of varying power extraction for varying heights in the turbine is necessary, since otherwise it would be possible to extract more energy from a layer than is physically present. For example, suppose (in a hypothetical extreme case), the wind speed were 0 m/s in the lowest layer intersecting the turbine and 10 m/s at hub height. Subtracting a portion of the total energy extracted from the lowest layer would be unphysical. Since wind speeds vary roughly logarithmically with height and the height of a turbine swept area is only D , higher wind power extracted at the turbine top are roughly compensated for by lower power extracted at the bottom.

For the RePower 5-MW turbine, a fit to the power curve data, combined with a correction for air density, was

$$P_{i,j,k} = \frac{\rho_a(T, P, q)}{\rho_{a,STP}} \begin{cases} 0 & W_{i,j,k} < 3.5002 \text{ m/s or } W_{i,j,k} > 30 \text{ m/s} \\ 807.69 + W_{i,j,k} \left(-495.51 + W_{i,j,k} (77.88 - 0.64 W_{i,j,k}) \right) & 3.5002 \leq W_{i,j,k} \leq 10 \text{ m/s} \\ 12,800 + W_{i,j,k} \left(-5713.3 + W_{i,j,k} (740.0 - 26.667 W_{i,j,k}) \right) & 10 < W_{i,j,k} \leq 13 \text{ m/s} \\ 5000 & W_{i,j,k} > 13 \text{ m/s} \end{cases} \quad (S4)$$

based on manufacturer-provided power output versus wind speed, where $\rho_{a,STP}=1.225 \text{ kg/m}^3$ is air density at standard temperature and pressure and $\rho_a(T,P,q)$ is air density at the current temperature (T), pressure (P), and specific humidity (q), all of which can vary substantially in a hurricane. The RE Power turbine power curve indicates a cut-in wind speed of 3.5 m/s, a designed cutout wind speed of 30 m/s, and a rated wind speed of 13 m/s.

For the Enercon E-126 7.58-MW turbine, a fit was

$$P_{i,j,k} = \frac{\rho_a(T,P,q)}{\rho_{a,STP}} \begin{cases} 0 & W_{i,j,k} < 3 \text{ m/s or } W_{i,j,k} > 34 \text{ m/s} \\ 221.7857 + W_{i,j,k} \left(-161.0913 + W_{i,j,k} (28.5119 + 2.2222 W_{i,j,k}) \right) & 3 \leq W_{i,j,k} < 12 \text{ m/s} \\ -36481 + W_{i,j,k} \left(7162 + W_{i,j,k} (-387 + 6.95 W_{i,j,k}) \right) & 12 \leq W_{i,j,k} \leq 17 \text{ m/s} \\ 7580 & 17 < W_{i,j,k} \leq 34 \text{ m/s} \end{cases} \quad (S5)$$

The E-126 power curve indicates a cut-in wind speed of 3 m/s a designed cutout wind speed up to 34 m/s, and a rated wind speed of 17 m/s. For both turbines, the designed cutout wind speed is below the maximum certified (destruction) wind speed of the turbine, 50 m/s. The purpose of cutout is to reduce loads on the blades, drive train, and tower at higher wind speeds. We model both an unmodified cutout speed (no additional loads) as well as a cutout wind speed near the maximum certified speed, the latter extracting more power at high wind speeds. To do this in practice would require strengthening and control modifications. Wind speeds above cutout occur rarely and, since wind turbines have been optimized only for power production, generation above cutout has not been considered worth the rare occasions of additional power production.

The final kinetic energy in each grid cell was $E_{Fi,j,k} = E_{li,j,k} - \Delta E_{i,j,k}$. The turbine also converted kinetic energy into turbulent kinetic energy (TKE) since the reduction in wind speed due to the turbine resulted in wind shear, creating subgrid-scale mechanical turbulence and TKE, which contributed to background turbulence (including from shear and buoyancy due to the hurricane itself). The TKE in both cases was calculated from the level 2.5 TKE closure scheme of (S32). The change in total kinetic energy in the grid cell due to power extraction by turbines was next partitioned proportionately among the kinetic energies of the surrounding u and v points, and the final wind speed at each u and v point was then extracted from the kinetic energy as described in the Supplementary Information of (S1).

Energy conservation due to power generation and frictional dissipation of winds at the surface was maintained in the model by converting all electric power generated by the wind turbines to heat where the electricity was used. The model also converted kinetic energy lost by natural surface roughness to turbulence and then heat. The electric power generated by turbines each time step, $\Delta E_{i,j,k}$, modified the surface air

temperature (where the electric power was consumed by human activity), as discussed in (S1).

S1.I. Simulations

Simulations were run for Hurricanes Katrina, Sandy, and Isaac, both without and with turbines. Simulations were initialized with reanalysis fields (S33). Katrina and Isaac simulations were run with one-way nested domains from the global to local scale with finest-domain resolution of $0.06^\circ \times 0.08^\circ$ (6 km x 8.8 km in the Gulf of Mexico).

Sandy simulations were run over a single continuous global-through-local stretched domain with finest resolution of 0.1° W-E x 0.1° S-N (approximately 8.5 km x 11 km offshore of the east coast), stretching to $4^\circ \times 5^\circ$ at the lowest resolution. Since the finest-longitude degree spacing on the domain was the same at all latitudes, part of the polar regions had $0.1^\circ \times 0.1^\circ$, grid spacing, which resulted in west-east distance spacing of ~ 0.7 km near the poles. As such, the dynamics time step was limited to 2 s or less. The stretched domain included 287 W-E x 189 S-N x 47 vertical layers = 2.55 million grid cells per simulation. Vertically, the model included 15 layers in the bottom one kilometer and remaining layers up to 60 km.

For the nested Katrina and Isaac simulations, the finest domain was 350 W-E x 150 S-N x 55 vertical cells (=2.89 million cells), including 15 vertical layers in the bottom one kilometer. The global domain in this case had an additional 13 layers (for a total of 68 layers) above the regional domain model top and had 72 W-E x 44 S-N horizontal cells. Between the two was a regional domain at 0.55° W-E x 0.5° S-N resolution covering 100 W-E x 80 S-N cells. For Katrina, Sandy, and Isaac, turbine blades were resolved vertically with five model layers (Figure S2).

The horizontal resolution was still somewhat coarse for idealistic hurricane simulation, thus certain turbulence structures, such as rolls (S34) may not have been resolved sufficiently in the horizontal. This may have caused some inaccuracies in the prediction of hurricane characteristics. Predictions of hurricane characteristics also depend significantly on initial horizontal wind and temperature fields (S35). Despite efforts to initialize the model with available data (S33), errors existed in these fields as well.

Hurricane Katrina simulations were run from 18 GMT August 28 to 2 GMT August 30, 2005. Hurricane Sandy simulations were run from 18 GMT October 29 to 0 GMT October 30, 2012. Hurricane Isaac simulations were run from 12 GMT August 28 to 20 GMT August 30, 2013.

In the case of the stretched-grid simulations, an advantage was the smooth, continuous transition from the large scale to the small scale. High-resolution limited-area models cannot account for this and must rely on boundary conditions that do not reflect true feedbacks. In the case of the nested and stretched-grid simulations,

advantages were the explicit size- and composition-resolved treatment of cloud, precipitation, and aerosol microphysics here (Sections S1.D, S1.E).

S1.J. Additional baseline hurricane model results

Figure 1 of the main text indicates that the modeled peak wind speeds and storm tracks were able to converge toward observed values within three hours of final land fall for Katrina and maintaining accuracy many hours after landfall. The model slightly overpredicted Sandy peak wind speeds and slightly underpredicted Isaac peak wind speeds, although not after landfall. Katrina and Isaac storm tracks were particularly accurate.

The normalized gross error (NGE, absolute value difference between model and data, all divided by data, then summed over all data points and divided by the number of data points) in modeled peak Katrina wind speed by GATOR-GCMOM, which does not assimilate data, accounting for all data points shown in Figure 1, was 7.7%. Comparatively, the NGE from the operational (data-assimilating) GFDL hurricane model (GHM) at coarse resolution was 25.0% and at fine resolution was 30.5% for Katrina.

For Sandy, the NGE of GATOR-GCMOM for all data points shown in Figure 1 was 14.7%. That from GHM-no-assimilation-coarse was 10.1%; that from GHM-no-assimilation-fine was 11.2%; that from GHM-with-assimilation-coarse was 12.9%; that from GHM-with assimilation-fine was 12.2%, and that from HWRF-with-assimilation was 2.3%.

For Isaac, the NGE of GATOR-GCMOM for all data points shown in Figure 1 was 9.8%.

Figures S3 and S4 compare GATOR-GCMOM 2-D wind speed field for Katrina and Sandy, respectively, with results from the GFDL (data-assimilating and non-data-assimilating versions) and HWRF (data-assimilating version) hurricane forecast models at a specific time. Figure S3 indicates similarities between GATOR-GCMOM results and results from the operational models. However, Figure 1 of the main text indicates that, for Katrina, the normalized gross error (NGE) of GATOR-GCMOM modeled peak wind speed relative to data in that figure was only 7.7%, less than the 25.0% and 30.5% NGEs for the GFDL operational coarse-resolution and GFDL operational fine-resolution models, respectively. For Sandy, the NGE was 14.7% for GATOR-GCMOM, which was a slightly greater error than from the other models.

S1.K. Treatment of wind turbine energy extraction

In order to test the impacts of wind turbines on energy extraction and storm surge reduction, two wind turbines (the geared RE Power 5 MW, with $D=126$ m rotor diameter and standard designed cutout wind speed (c_o) =30 m/s and the gearless Enercon E-126 7.58 MW, with $D=127$ m and standard $c_o=34$ m/s) were incorporated into the model under different conditions. These included for array spacing of $4D \times 7D$ and the designed cutout wind speed; array spacing of $4D \times 7D$ and the cutout wind speed raised to the maximum certified wind speed of 50 m/s; and array spacing $4D \times$

14D with $c_o=50$ m/s. In all cases, turbines were placed within 100 km of the coast. For Hurricane Katrina, turbine arrays were placed along a long stretch of the gulf coast between 22.5-32 N and 81.5-95 W. An additional simulation was run in which turbines were placed only to the southeast of New Orleans (87.5-89.5 W). For Hurricane Sandy, turbines were placed between 35-44 N and 65-78 W. An additional simulation was run with arrays between Washington D.C. and New York City only (38.8 N to 41 N). For Hurricane Isaac, turbine arrays were placed to the southeast of New Orleans only (87.5-89.5 W). Table 1 of the main text summarizes the installed densities, number of turbines, and nameplate capacities for the nine cases tested. Figure S5 indicates that the water depth in these regions is mostly <30 m but up to 50 m in some areas and 200 m in other areas. Use of all these regions together is a simplification for model setup. With current technologies, offshore wind costs the least in waters shallower than 30 m, so initial developments will be done there. Waters deeper than 60 m are currently too expensive to develop but could readily be developed with the expansion of floating turbines, currently being tested.

In one case, arrays filled the offshore area from DC to NY with 112,014 turbines for a total installed capacity of 849 GW, with estimated average delivered power of 316 GW. A prior analysis of approximately this installed capacity (834 GW) of 5-MW turbines off the Mid-Atlantic Bight estimated average delivered power of 330 GW, enough to run Massachusetts through North Carolina electricity, light vehicles, and building heat (S36).

The reason for testing different cutout wind speeds is as follows. The International Electrotechnical Commission (IEC) and the Germanischer Lloyd classification society specify design requirements to protect wind turbines from damage throughout their working lifetimes. Under the most strenuous standard, IEC 61400-3 classified turbines are designed to withstand a 10-minute sustained wind speed of at least 50 m/s (S37). Current designed cutout wind speeds for the sample turbines are 30-34 m/s. Upon reaching the designed cutout wind speed, the turbine is shut down to minimize damage and lengthen its life. Here, we test whether keeping the turbines running at the rated wind power between the designed cutout wind speed and the maximum certified wind speed helps more to weaken a hurricane. As noted above, this does not mean that the two turbines assumed could be used without modification for this purpose. Instead, they would need to be redesigned to have operating modes at higher wind speeds to slow the winds while presumably generating power and simultaneously staying protected from excess forces on structural components.

According to (S40) and (S39), which corrected the article (S38), a 5% possibility may exist that one-fifth of turbines that do not yaw in a hurricane prone region, such as Galveston, Texas, may be damaged sometime during a 20-year period. However, modern horizontal-axis turbines are designed to yaw, and yaw failures are uncommon. Furthermore, turbines located along the Atlantic coast face virtually no chance of hurricane wind damage due to slower hurricane winds there, almost all below the maximum certified wind speed of currently-designed turbines of 50 m/s. Further, as shown here, if the turbine array is large enough, wind speeds near

turbines are slower than in the absence of the turbines, so the probability of damage decreases further. Turbines first see the outer-rotational winds of a hurricane, which are slower than eye-wall winds, and dissipate the hurricane from the outside-in. Finally, it is possible to strengthen turbines so as to reduce the chance of damage, and to increase the wind speeds for which they could be certified.

The 4D x 7D spacing used in some simulations here has been used offshore in Europe, but is more compact than is currently being planned for US offshore wind facilities. This is a reason wider spacing (4D x 14D) is also tested. The advantages of closer spacing are that it reduces hurricane wind speeds and intra-array transmission collector cabling more and makes better use of ocean space. However, it leads to upstream turbines taking more wind than downstream ones during normal operation, thus raising the cost of power. Additionally, the layouts simulated here just fill the area, without considering exclusion zones or shipping rights of way. These inputs to the simulation—tighter spacing, filling the continental shelf, and largest turbine counts—are beyond what would normally be planned for commercial offshore wind facilities for reason of cost. Also, increasing the cutout speed to 50 m/s while still extracting energy will be challenging and has not yet been put into practice through an engineering design. These scenarios are tested because the purpose of this study is to model the hypothesized potential for arrays of turbines to mitigate damage. If the potential is found, then more specific strategies, layouts, and turbine design modifications should be explored.

In the scenarios developed here, the arrays of turbines will generate large amounts of power during the year. As noted above, even the smaller arrays will supply most of the east and southern coast electricity demands. During hurricanes, wind turbines will generate more electric power than average if the generator is engaged during such high winds. Prior studies have shown how to manage large amounts of power from U.S. East Coast offshore wind and how best to use it when it exceeds local electrical loads, for example through undersea or overhead transmission out of the area, by electrifying heating and vehicles, or by generating hydrogen (*S41, S42*).

S1.L. Storm surge calculation

Storm surge is the sea level rise that occurs upon storm landfall. Flooding from it is generally responsible for the most casualties in a storm. Storm surge is caused mainly by continuous high winds offshore pushing ocean water toward land, where the water piles up. Storm surge increases primarily with increasing wind stress (thus proportionally to the square of wind speed) and decreasing water depth. Secondary mechanisms include the effects of low pressure in the hurricane's center, the Coriolis force, ocean waves, fetch (proportional to the square of wind speed), storm size, and rainfall.

Storm surge h (m) is approximately related to wind speed V (m s^{-1}), fetch F (m), and bathymetry H (m) by (*S43*)

$$h = C \frac{\tau_{SFC} F}{g \rho_{WATER} H} = C \frac{C_D \rho_{AIR} V^2 F}{g \rho_{WATER} H} = k \frac{V^2 F}{H} \quad (S6)$$

where ρ_{AIR} and ρ_{WATER} are air and water densities (1.23 and 1025 kg m⁻³, respectively), τ_{SFC} is the wind stress at the surface, g is gravity (9.81 m s⁻²), C_D is the drag coefficient (2×10^{-3}), C is a constant ($1 < C < 1.5$, here 1.35), and k is a derived constant (3.32×10^{-7} s² m⁻¹) (S44, S45, S46). Because the fetch calculated in Equation S6 will depend on the radial distance between the core and the location of maximum winds, it will depend on storm size, a factor relevant for determining storm surge (S47). In order to ensure the storm surge in the base cases (without turbines) equaled observed storm surge upon landfall in the cities of interest (4.2 m in New Orleans for Katrina, 3.8 m in New York City for Sandy, and 2 m in New Orleans for Isaac), H was back-calculated in the base case simulations to equal 35 m for Katrina, 14.3 m for Sandy, and 29 m for Isaac. These values were used for all times for both the baseline and sensitivity simulations for each hurricane.

With turbines, storm surge h_{WITH} is reduced from its value without turbines ($h_{WITHOUT}$) by a fraction Δh equal to

$$\Delta h = 1 - \frac{h_{WITH}}{h_{WITHOUT}} = 1 - \frac{V_{WITH}^2 F_{WITH}}{V_{WITHOUT}^2 F_{WITHOUT}} \quad (S7)$$

Equation S6 was obtained from the depth-integrated wave equations with frictional effects solved for a narrow channel of uniform depth H (m) and length F (m) under uniform wind speed V (m/s) (S44, S45, S46). Although the conditions during a hurricane are far more complex than those in a channel, simplified equations similar to, or simpler than Equation S6 have been used, including operationally, to predict the maximum surge based on only a few hurricane parameters, such as maximum wind speed, storm speed, lowest pressure, and local water depth (S48, S49, S50), before the advent of predictive numerical models (e.g., S51). Most such equations show a dependency with wind speed that is of the form V^a , with $a > 3/2$ in all cases and $a = 2$ in most cases. Therefore, the use of a simplified equation appears justified in the literature and for the present purpose, but we apply it over time and consider the entire 2-D surface wind field and bathymetry data (Figure S5). Equation S6 takes into account not only the direct wind speed effect, but also the wave effect by accounting for fetch and the Ekman spiral effect by accounting for water depth H . As such, Equation S6 appears to be more comprehensive than most past simplified equations.

We use Equation S7 as the basic equation to predict the storm surge change due to wind turbine arrays, but to make it applicable to the atmospheric and oceanic conditions that occur during a hurricane, we add the following assumptions:

i) V^2 in Equations S6 and S7 is the average squared wind speed over the hurricane sector in which the wind direction is toward the location of interest. For Sandy, the location of interest is New York City and for Katrina it is New Orleans. Table S1 lists

the coordinates of the sectors in each scenario as a function of time. We calculate the sector-average squared wind speed during all hours around landfall and use the range of resulting values to generate the range of storm surge reductions reported in Table S1.

Table S1. Parameter values for storm surge calculations for each model simulation¹.

	Katrina					Sandy					Isaac	
	Base	(A) Most of gulf coast	(B) Most of gulf coast	(C) Most of gulf coast	(D) New Or- leans only	Base	(E) Much of east coast	(F) Much of east coast	(G) Much of east coast	(H) DC to NYC only	Base	(I) New Or- leans only
Highest wind ² (m/s)	53.7 (58.1)	53.8 (62.8)	52.0 (57.9)	50.7 (57.9)	55.5 (57.9)	55.2	52.3	46.6	49.8	53.8	42.2	42.2
V_{MAX} (m/s)	51.8	48.6	48.4	48.2	50.7	50.1	42.3	42.6	42.6	46.2	40.6	40.6
V_{FM} (m/s)	7.0	7.1	7.2	7.1	7.2	8.3	8.7	8.5	9.2	8.7	4.0	4.2
R_{MAX} (km)	113	164	122	131	188	225	268	235	210	289	93	125
F (km)	451	471	439	448	495	485	428	426	386	466	381	410
$(V^2)_{AVG}$ (m ² /s ²)	305- 1015	118- 742	154- 809	121- 754	152- 836	339- 566	255- 485	308- 526	288- 515	274- 511	168- 452	125- 295
Storm surge (m)	1.3- 4.3	0.5- 3.3	0.6- 3.4	0.5- 3.2	0.7- 3.9	3.8- 6.3	2.3- 4.8	2.9- 5.2	2.6- 4.6	2.9- 5.5	0.7- 2.0	0.6- 1.4
Δ Storm surge (Δh , %)		23-79	19-63	26-75	6-71		24-34	17-21	27-32	12-21		18-60

¹For Katrina, the sector coordinates for the storm surge calculation were as follows: $t \leq 6$ GMT: 28.5N-30.5N and 89.5W-87W; $t = 10$ GMT: 29N-30.5N and 89.5W-87W; $t \geq 14$ GMT: 29.5N-30.5N and 89.5W-87W. For Sandy, they were as follows: $t \leq 21$ GMT: 39N-41.5N and 74W-71W; $t = 22$ GMT: 39.5N-41.5N and 74W-71W; $t \geq 23$ GMT: 40N-41.5N and 74W-71W. For Isaac, they were as follows: for $t = 12$ GMT: 29.0N-30.5N and 89.5W-88W; $t > 12$ GMT: 29.0N-30.5N and 90W-88W.

²The first number is the highest wind speeds in the region of interest (around New Orleans New York, and New Orleans for Katrina, Sandy, and Isaac, respectively). The number in parentheses for Katrina is the highest wind speed anytime during the simulation in the whole domain (e.g., as in Figure 1 of the main text).

ii) The fetch is obtained from (S46) as follows:

$$F = F_{30} \left[\log_{10} \left(\frac{R_{MAX}}{30 \times 10^3} \right) + 1 \right] \quad (S8)$$

where R_{MAX} is the radial distance from the core to the location of maximum wind speed in the hurricane (km) and F_{30} is the fetch of a “standard” hurricane with $R_{MAX} = 30$ km, calculated from

$$F_{30} = aV_{MAX}^2 + bV_{MAX}V_{FM} + cV_{FM}^2 + dV_{MAX} + eV_{FM} + f \quad (S9)$$

In this equation, V_{MAX} (m s⁻¹) represents the average wind speed in the strongest sector of the hurricane at its peak intensity during the simulation, rather than the

absolute highest wind speed from a single grid cell (which is also reported in Table S1 for completeness). Note that the simulated highest wind speed initially differed from the observed highest wind speed because the simulation started from a reanalysis field that did not match the observed fastest winds or lowest pressure. However, by three hours prior to final landfall the modeled hurricane caught up and matched the peak wind speeds of the observed hurricane (Figure 1 of the main text). To determine V_{MAX} , each time step, starting from the beginning of the simulation until landfall, we calculate the average of the 25 highest wind speeds in the hurricane, which can be “patchy” and scattered due to convective activity, and assign the highest of those averages to V_{MAX} . V_{FM} is the storm speed (m s^{-1}) during the eight- or four-hour interval prior to final landfall (for Katrina and Sandy respectively, due to their different output time resolution), $a = -6.525 \times 10^1$, $b = 4.518 \times 10^2$, $c = -3.669 \times 10^3$, $d = 6.570 \times 10^3$, $e = 2.021 \times 10^4$, and $f = 2.394 \times 10^4$. To calculate V_{FM} , the coordinates of the 25 grid points with the lowest pressures are averaged to identify the storm center each time step. Then the storm speed is obtained at each time step as the distance between the storm center positions over the current and the previous time steps. Because there are 25 radii to maximum wind speeds each time step, their average is calculated each time step and the highest average value is then assigned to R_{MAX} , analogously to the assignment of V_{MAX} .

iii) Whereas one value of the fetch from Equation S8 is used for all hours in Equations S6 and S7, a different value of V^2 is used for each time step to obtain the range of storm surge values reported in Table S1. The storm surge changes in Table S1 are similarly a range determined over all time steps of the simulation, not just upon landfall.

Despite the simplicity of this storm surge calculation, it is both physically-based and forced by observations, so has zero error by design in predicted storm surge in the city of interest upon landfall. This is accomplished by back-calculating an effective bathymetry H in Equation S6, which generates an exact value for the observed storm surge in New Orleans, New York City, and New Orleans, upon landfall of Hurricanes Katrina, Sandy, and Isaac, respectively. In addition, the method produces reasonable estimates of the various hurricane parameters shown in Table S1. For example, the radius to maximum winds R_{max} was estimated for Katrina to be 113 km and for Sandy, 225 km, almost matches to the observed 110 km and 238 km, respectively. Isaac had the smallest observed R_{max} among the three hurricanes analyzed here (40-45 nm, 74-83 km), not far from our estimate of 93 km. Also the speed of forward momentum V_{fm} calculated with the proposed method was remarkably accurate. Isaac was the slowest of the three hurricanes, as correctly shown in the calculated V_{fm} values (4 m/s calculated, 3.6 m/s observed). Katrina’s observed V_{fm} was 6.7 m/s, very close to our estimate of 7 m/s). Sandy was the fastest among the three hurricanes considered here, as correctly forecasted with our method (8.3 m/s), although it was modeled to move slightly slower than observed.

S2. Supporting Cost Analysis

Table 2 of the main text presents a simplified cost-benefit analysis of development of offshore turbine arrays to protect New Orleans alone (Simulation D) and, separately, Maryland, Delaware, New Jersey, and New York (Simulation H). The avoided hurricane costs were calculated as described in the footnotes to Table 2. Briefly, avoided costs included those related to storm surge damage and those related to wind damage. The damage reduction as a function of storm surge reduction was determined from (S52). The damage reduction as a function of wind speed reduction was determined from (S53).

Overall avoided hurricane damage costs were estimated at 0.21-0.68 ¢/kWh for New Orleans and 0.09-0.13 ¢/kWh for the East Coast over the lifetime of the turbines. The avoided damage cost equaled the per-hurricane cost (\$81.2 billion due to Katrina and \$82 billion due to Sandy) multiplied by the number of hurricanes over the life of the turbines (2.7 hurricanes over a low-estimate 20-year lifetime and 4.1 over a high-estimate 30-year lifetime for Katrina and 1.5 over a 20-year lifetime and 2.3 over a 30-year lifetime in the case of Sandy) divided by the turbine lifetime and by the energy generated during the turbine lifetime. The future values are not discounted to present cost. The number of hurricanes per 20-30 years is estimated from Table S2, which shows the number of hurricanes of different class size by state and region from 1850-2006. The table indicates that New York hurricanes averaged 1.5 or 2.3 hurricanes per 20- or 30-year period, respectively. For Sandy, we assume this range per life of the turbine. Gulf coast hurricanes average 4.9 or 7.4 per 20- or 30-year period (Table S2). However, wind arrays that we propose to protect individual regions would be about the width of Mississippi's coastline (71 km), and that state has experienced 2.7 or 4.1 hurricanes per 20 or 30 years. This is used as the range in the number of hurricanes per turbine 20- or 30-year lifetime for the cost analysis.

The normal delivered power generated per turbine over its life in Table 1 was determined by summing the product of the power output from the Enercon-126 7.58-MW turbine at a given wind speed, the probability of the wind speed over the year, and the number of hours per year, over all possible wind speeds. The power output for the turbine versus wind speed was determined from Equation S5 and the probability of each wind speed was assumed to be Rayleigh-distributed with mean values of 8.5-9 m/s.

Table S2. Frequency of coastal hurricanes by state from 1850-2006 (S54).

State	Cat 1	Cat 2	Cat 3	Cat 4	Cat 5	Total	Total per 20 years	Total per 30 years
Maine	5	1	0	0	0	6	0.77	1.2
New Hampshire	1	1	0	0	0	2	0.26	0.39
Massachusetts	5	2	3	0	0	10	1.3	1.9
Rhode Island	3	2	4	0	0	9	1.2	1.7

Connecticut	5	3	3	0	0	11	1.4	2.1
New York	6	1	5	0	0	12	1.5	2.3
North Atlantic							1.1	1.6
New Jersey	2	0	0	0	0	2	0.26	0.39
Delaware	2	0	0	0	0	2	0.26	0.39
Maryland	1	1	0	0	0	2	0.26	0.39
Mid Atlantic							0.26	0.39
Virginia	5	2	1	0	0	8	1.0	1.5
North Carolina	21	14	11	1	0	47	6.1	9.1
South Carolina	17	7	4	2	0	30	3.9	5.8
Georgia	6	5	2	1	0	14	1.8	2.7
Southeast Coast							3.2	4.8
Florida	43	34	29	6	2	114	14.7	22.1
Florida							14.7	22.1
Alabama	11	5	5	0	0	21	2.2	3.3
Mississippi	2	6	8	0	1	17	2.7	4.1
Louisiana	19	15	16	3	1	54	7.0	10.5
Texas	24	18	12	7	0	61	7.9	11.8
Gulf Coast							4.9	7.4

The greater damage cost avoidance benefit to New Orleans occurred because the arrays were focused only in a sector to the southeast of the city rather than along a long coastline, thus fewer turbines were needed to reduce a similar level of damage. The turbines also reduce 2010 air pollution health and climate costs by ~5.3 ¢/kWh by displacing power, thus emissions, from power plants near populated areas.

An extensive survey of existing offshore wind projects shows an average price of 19¢/kWh (assuming no subsidies, capex of \$4250/MW, tax rate of 35%, net capacity factor (CF) of 36%, either corporate (7.8%) or project (15%) finance cost) (\$55). To estimate costs for a large build like that envisioned here for protection from hurricanes, the comparison price would not be the 19¢/kWh historical average, but would be better estimated from that cost survey's "best recent project cost" of 9.4¢/kWh (accounting for installation, operation, maintenance, scrapping), which is the cost for better managed projects in a still-immature industry. The "best recent cost" assumes no technology improvements in the future whatsoever, which we judge very unlikely for a build of the size envisioned, thus we consider 9.4¢/kWh as a realistic cost projection for winds offshore New York, even though it is well below current average practice, and a higher cost (Table 2) off of New Orleans, due to lower wind speeds there. Table 2 puts costs and benefits into a cents per kWh metric, comparing hurricane protection as if it were an avoided cost (e.g., a benefit) of the production of electricity from offshore wind.

Offshore wind turbines strengthened to withstand hurricanes better or modified for a higher cutout wind speed would cost more than this, and possibly significantly more. Thus it is relevant that our simulation that assumed no change in cutout wind speed gave almost as much reduction in storm surge as our simulation assuming a cutout speed equal to the maximum certified wind speed. Similarly, it is important that most storms along the East Coast in particular do not exceed the rated 50 m/s rated speed for production Class I turbines. However, economies of scale and better materials are also expected to reduce the per-turbine cost so that stronger turbines may, over time, become cost-competitive.

Upon including benefits but no tax or other subsidies, the net cost of offshore wind is ~4-8.5¢/kWh, which compares with new fossil-fuel generation costs in these areas of ~10¢/kWh. Looking at each value in Table 2, the cost of generation alone is roughly similar between a mature offshore wind industry and current generation. The health and pollution benefits significantly reduce the wind cost, and the hurricane protection, given our value of prevented damage assumptions, adds a smaller benefit. Since power decisions are made by states, in a political environment with participation by health advocates, coastal protection, and legacy generation interests, it is of value to show that each factor contributes to cost and/or value.

Overall, we find here that large arrays of electricity-generating offshore wind turbines may diminish hurricane risk cost-effectively while reducing air pollution and global warming and providing local or regionally-sourced energy supply. The net cost would be significantly less than the cost of continuing to build fossil generation in these regions.

Some additional factors not considered here include the possibility of some zones of enhanced turbulence due to changes in the flow caused by turbines and the impacts of arrays of turbines on other ocean uses, such as shipping routes. While these issues are practical and need to be addressed if large turbine arrays are put in place, prior studies suggest that they are manageable, not insurmountable barriers or risks.

S3. Supporting Figures

Figure S1. Some aerosol-cloud microphysical processes in GATOR-GCMOM. Size- and composition-resolved liquid and ice particles grow by nucleation and condensation/deposition of water vapor onto all size- and composition-resolved aerosol particles simultaneously while accounting for Köhler theory (assuming the Kelvin effect and Raoult's law affect the equilibrium saturation ratio over liquid water whereas only the Kelvin effect affects that over ice). Interstitial aerosol particles coagulate with the hydrometeor particles, and the hydrometeor particles coagulate among themselves to form larger hydrometeor particles of the same type or to produce graupel (a combination of liquid and ice particles that become frozen). Hydrometeor collisions also result in breakup and bounceoff, either splitting up hydrometeor particles or separating charge for lightning formation. All aerosol constituents are tracked in the hydrometeor particles of each size. Hydrometeor particles fall, with the largest becoming precipitation. As they fall, they evaporate/sublimate, releasing aerosol cores and water vapor back to the air in some cases and falling to the surface in others. Evaporation below the cloud causes cooling, enhancing downdrafts; condensation causes warming, creating buoyancy and enhancing updrafts. Hydrometeor particles that fall over snow and sea ice retain their aerosol cores and affect the radiative properties of the snow and ice. From (S16).

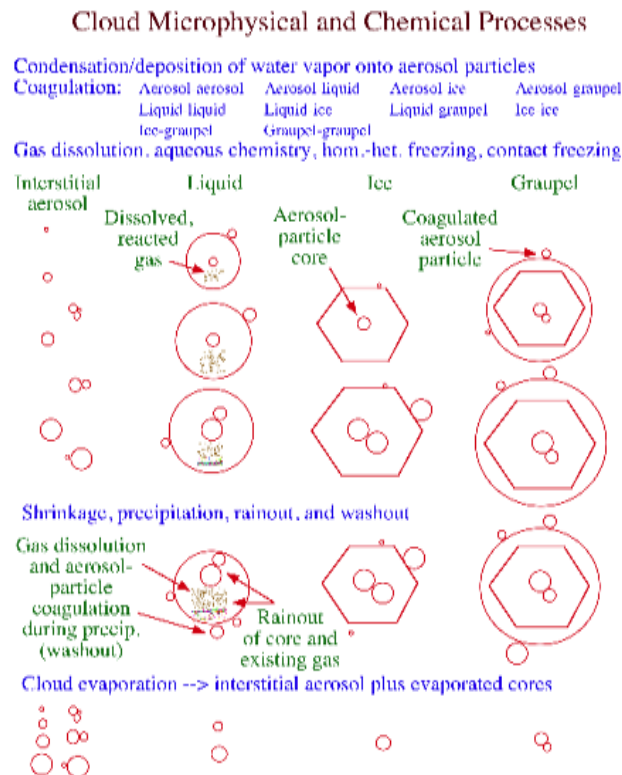


Figure S2. Illustration of how the swept area of a single wind turbine intersects multiple model vertical layers in a single grid column. Points A, B, C, D, and H are discussed in the text.

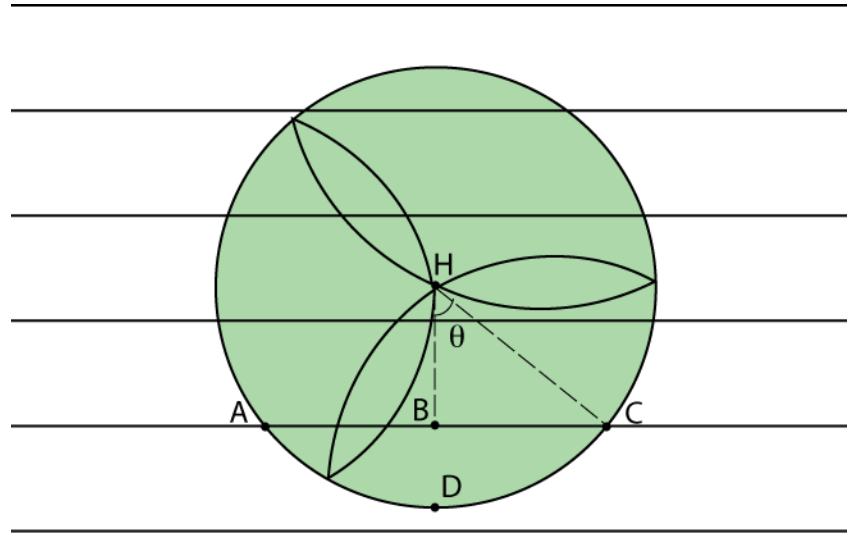


Figure S3. Snapshot comparison of wind speed field (m/s) for Hurricane Katrina on August 29, 2005 at 6 GMT among three models (GATOR-GCMOM, GFDL operational coarse, and GFDL operational fine). The operational models assimilated data. The coarse had $0.167^\circ \times 0.167^\circ$ resolution and the fine one had $0.083^\circ \times 0.083^\circ$ resolution. Figure 1 of the main text compares the modeled peak wind speed at this time with data for each of the three models.

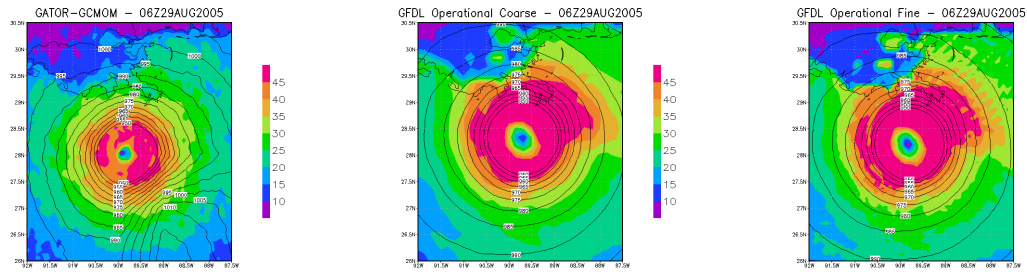


Figure S4. Snapshot comparison of wind speed field (m/s) for Hurricane Sandy on October 29, 2012 at 21 GMT among three models (GATOR-GCMOM, GFDL operational coarse, and GFDL operational fine). The operational models assimilated data. The coarse one is at $0.167^\circ \times 0.167^\circ$ resolution and the fine one is at $0.083^\circ \times 0.083^\circ$ resolution.

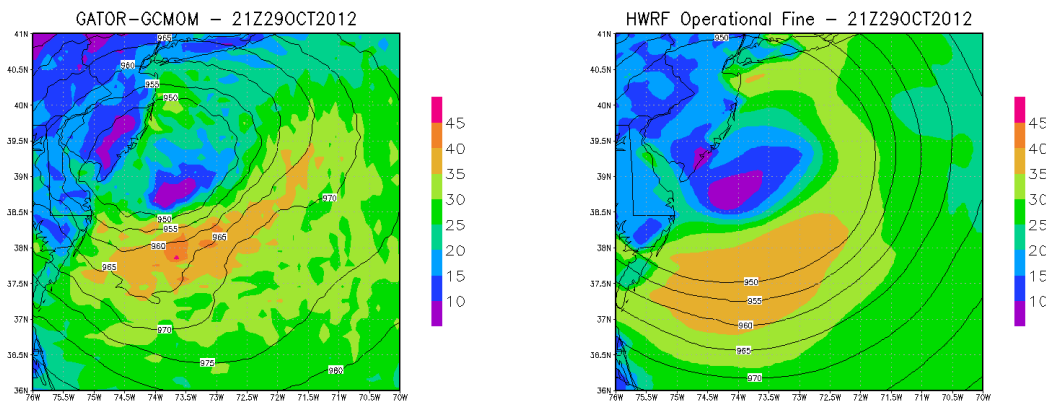


Figure S5. Topography and bathymetry map for the (a) gulf coast and (b) east coast. Data from (S56). Colors indicate bathymetry depth from 0-200 m.

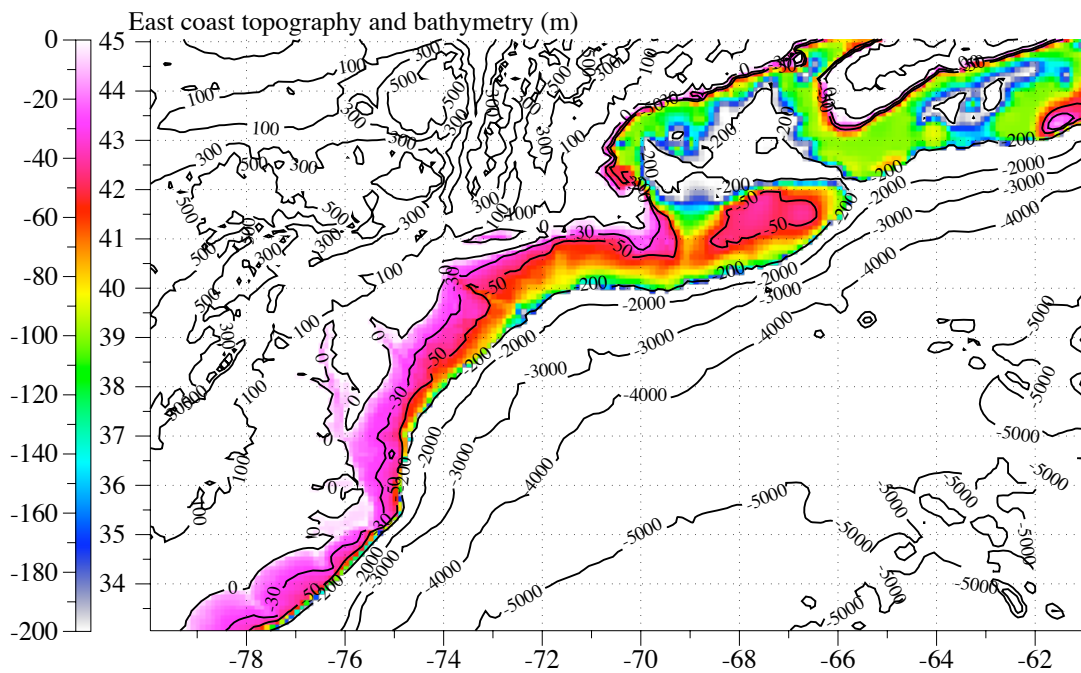
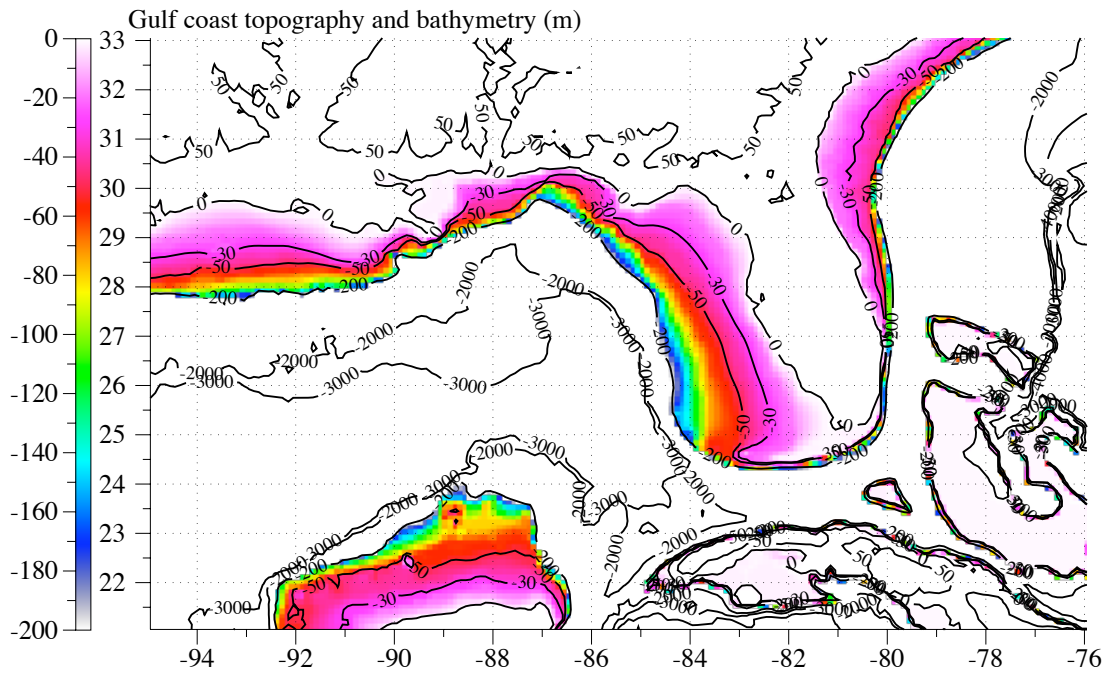


Figure S6. Snapshot 15-m wind speeds from simulations of Hurricane Katrina in the absence (top left) and presence (top middle) of arrays of wind turbines within 100 km of land (Simulation A in Table 1 of the main text). The top right panel shows the difference in 15-m wind speed between the two plots. The wind speed reduction resulted from power extraction by the wind turbines (bottom left). The bottom right panel shows the pressure difference due to adding turbines. The turbines assumed were 7.58-MW turbines with rotor diameter (D) of 127 m and hub height of 100 m. Spacing was $4D \times 7D$. The simulation was started at 18 GMT August 28, 2005, with the hurricane extant. The contours are bathymetry between 0-200 m depth.

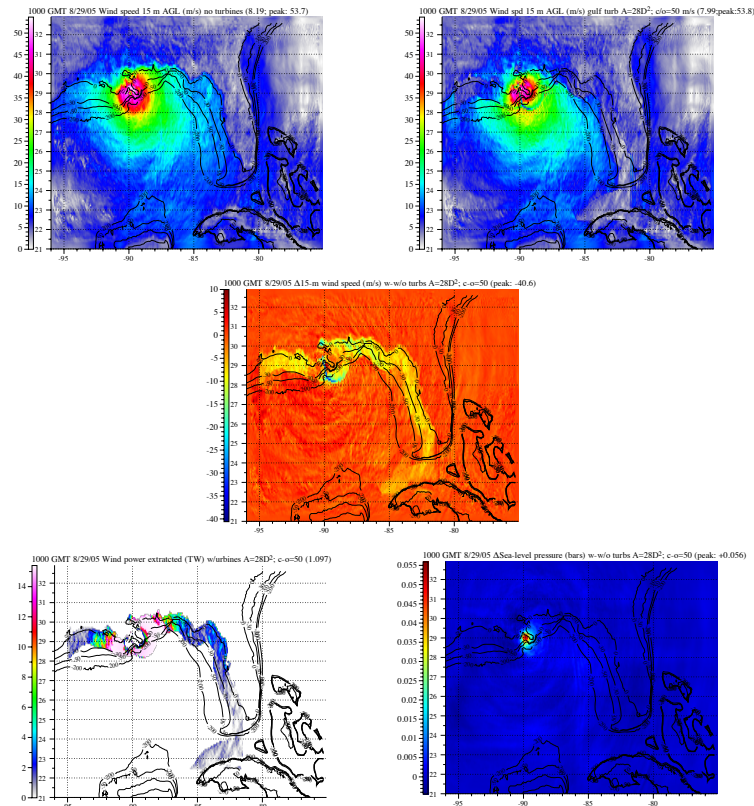


Figure S7. Snapshot 15-m wind speeds from global-through-local stretched-grid simulations of Hurricane Sandy in the absence and presence of arrays of wind turbines within 100 km of land (Simulation E in Table 1 of the main text). The difference in 15-m wind speed between the two plots is also shown. The wind speed reduction results from power extraction by the wind turbines (right figure). The turbines assumed were Enercon E-126 7.58-MW turbines with rotor diameter (D) of 127 m and hub height of 100 m. Spacing was $4D \times 7D$. The simulation was started at 18 GMT October 29, 2012, with the hurricane extant. The contours (when shown) are bathymetry between 0-200 m depth.

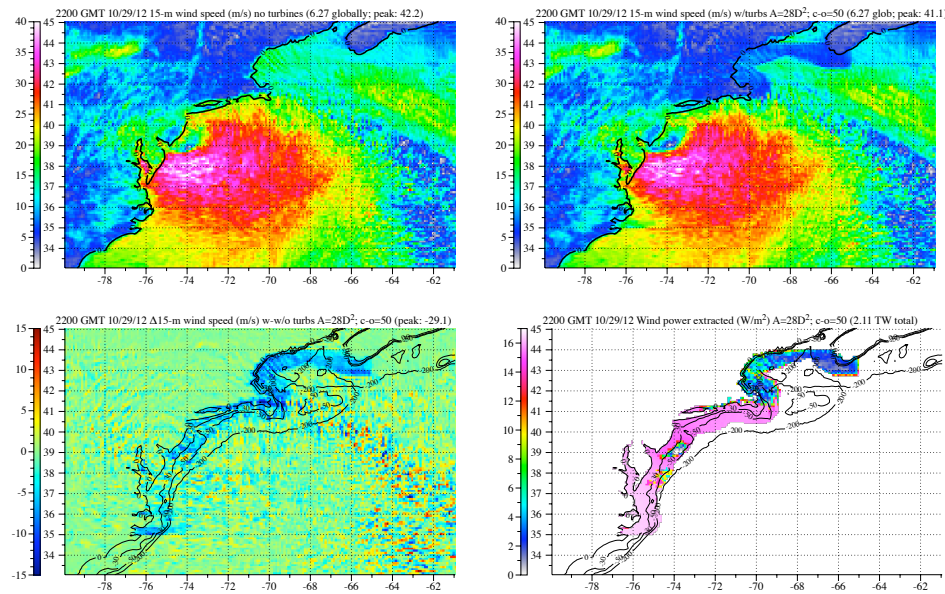
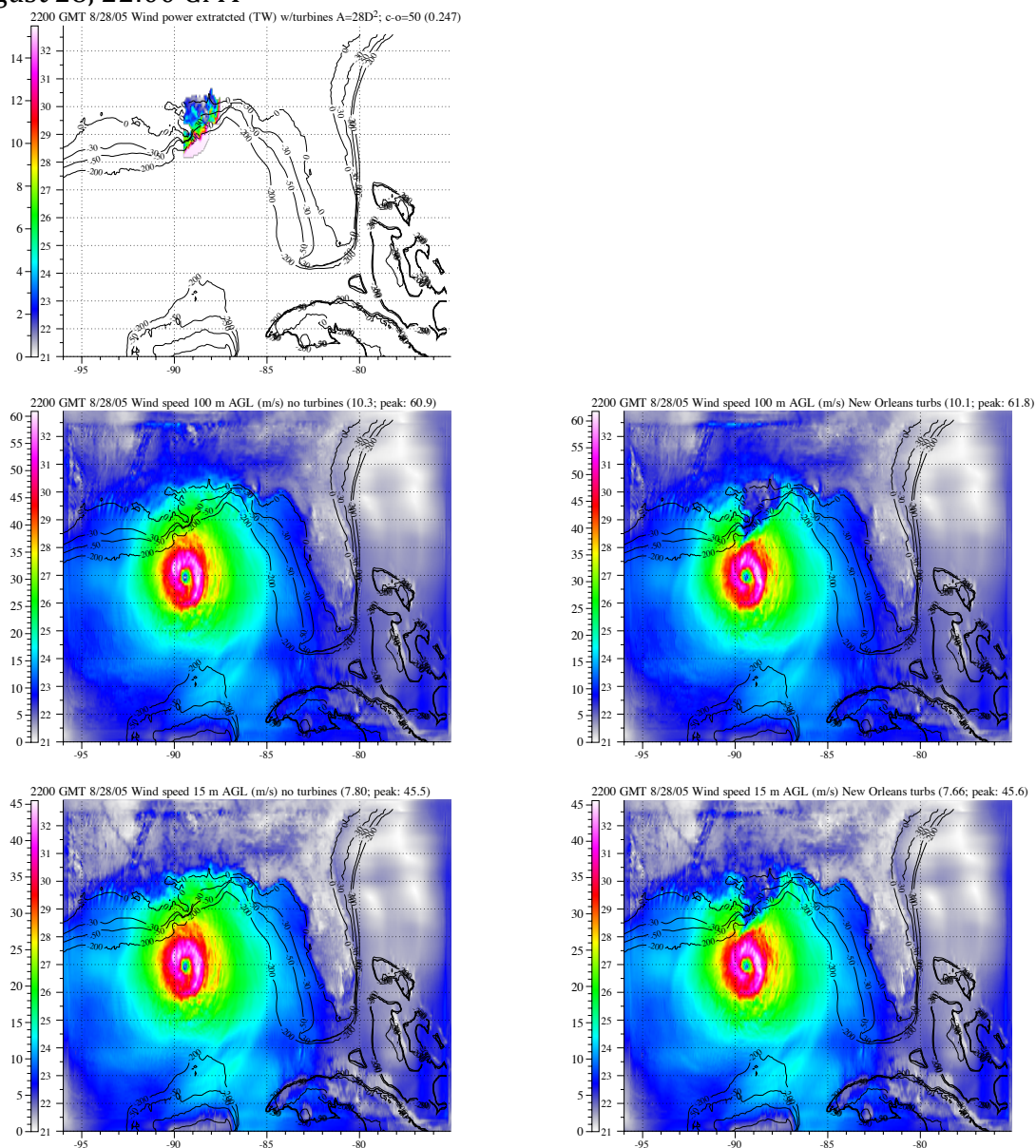
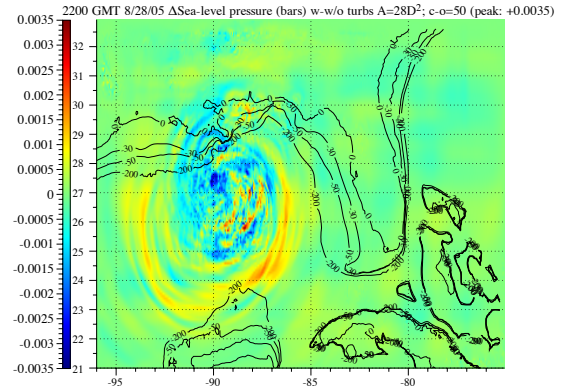
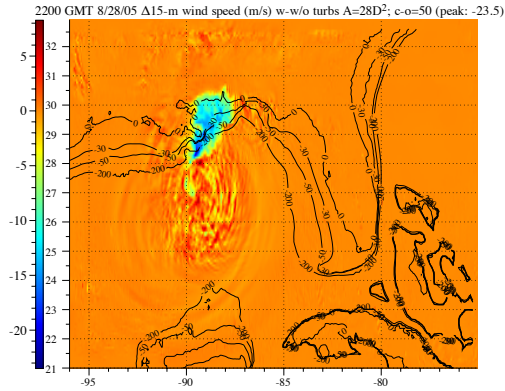


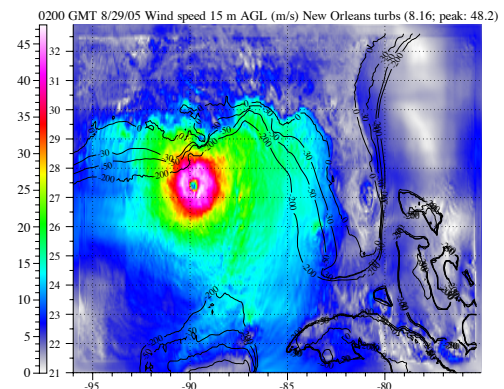
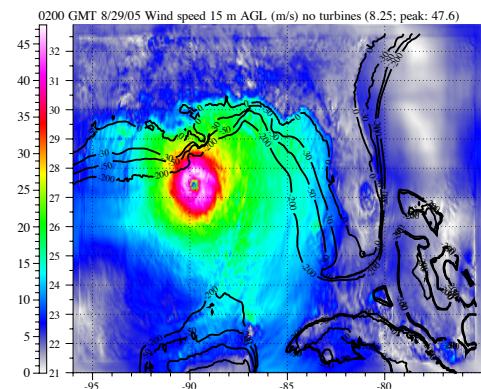
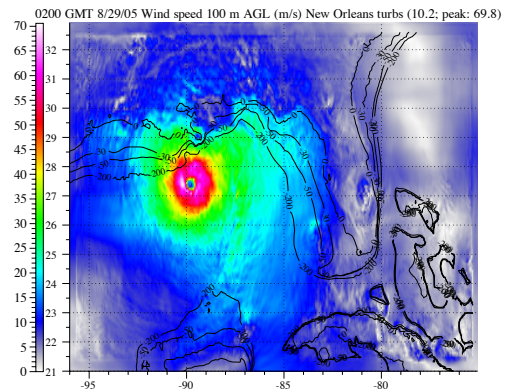
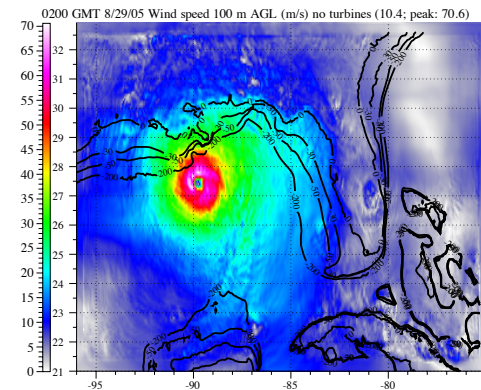
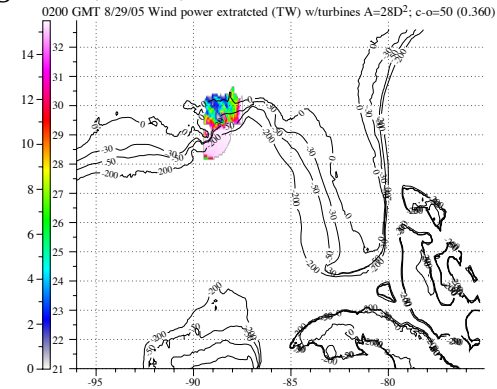
Figure S8. Time series of instantaneous power extraction (TW), 100-m wind speeds (m/s) in the absence and presence of turbines, 15-m wind speeds (m/s) in the absence and presence of turbines, 15-m wind speed differences (m/s) with minus without turbines, and sea-level pressure with minus without turbines offshore of New Orleans during Hurricane Katrina based on global-through local nested simulations (Simulation D in Table 1 of the main text). The turbines assumed were Enercon E-126 7.58-MW turbines with rotor diameter (D) of 127 m and hub height of 100 m. Spacing was $4-D \times 7-D$, and turbines were placed within 100 km of shore in front of New Orleans between 87.5 - 89.5 W (Simulation D in Table 1 of the main text). The simulation was started at 18 GMT August 28, 2005, with the hurricane extant. The contours are bathymetry between 0-200 m depth.

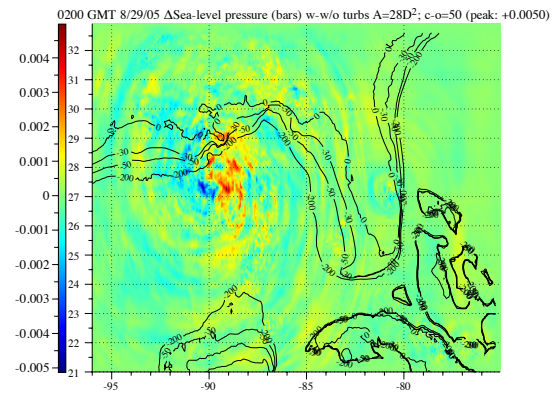
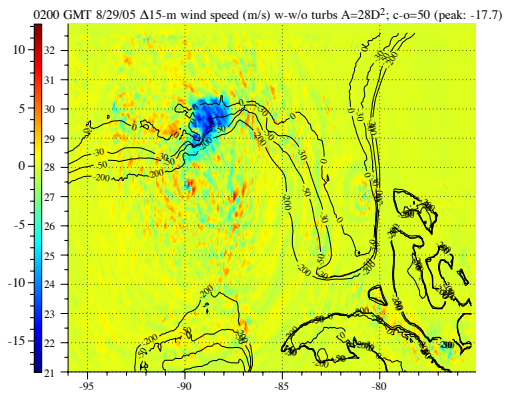
August 28, 22:00 GMT



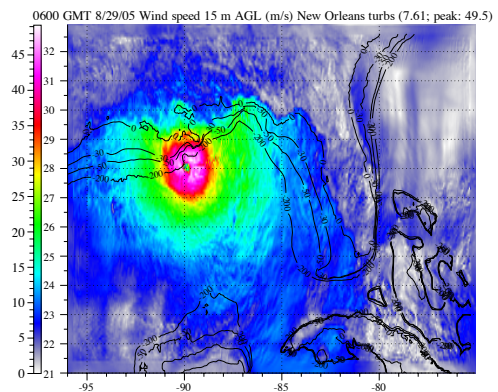
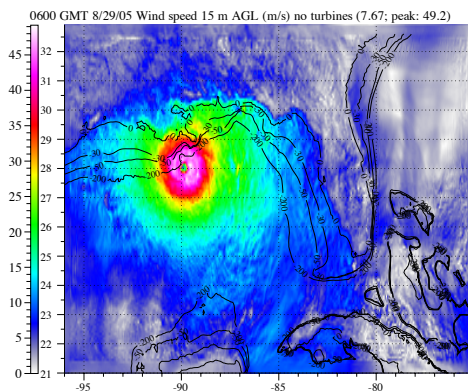
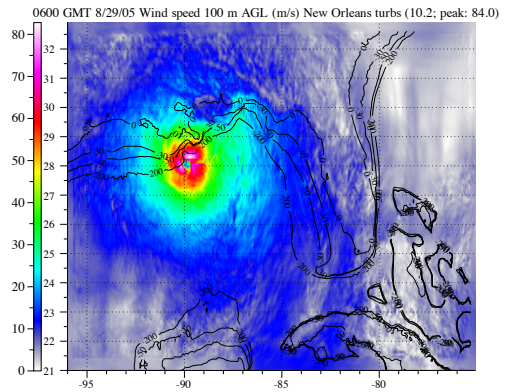
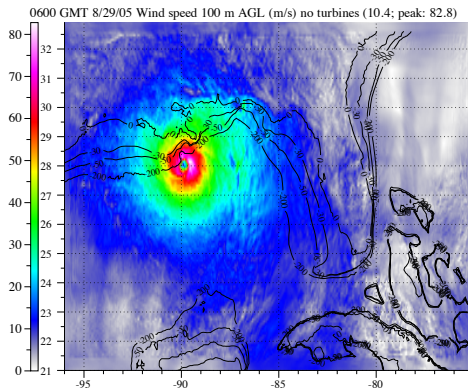
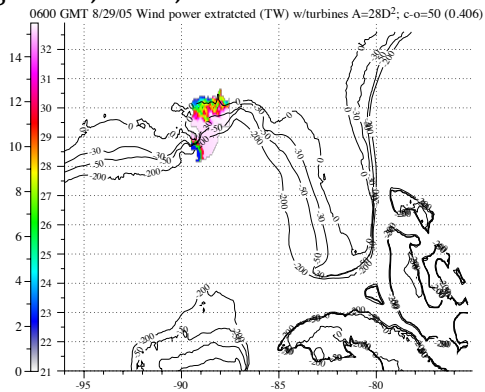


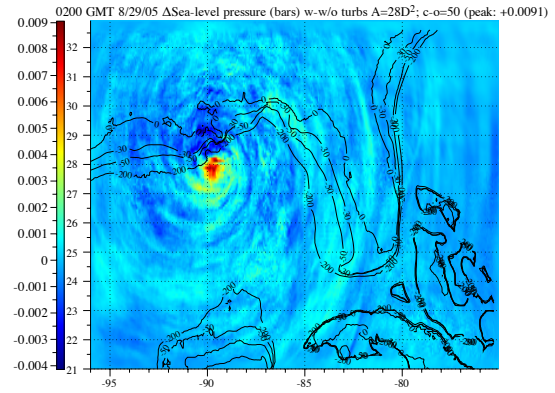
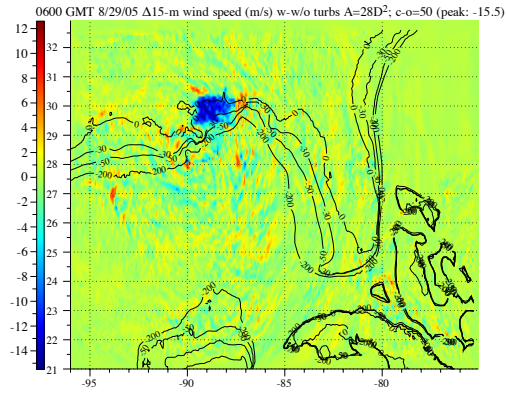
August 29, 2005, 02:00 GMT



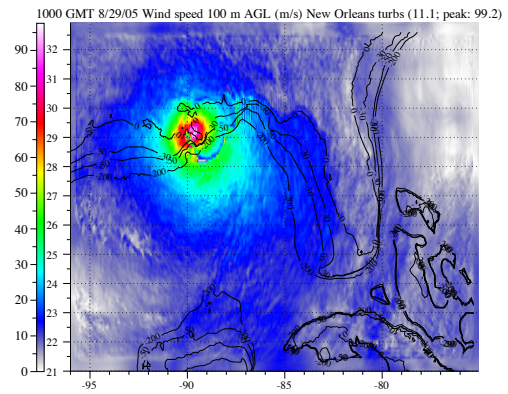
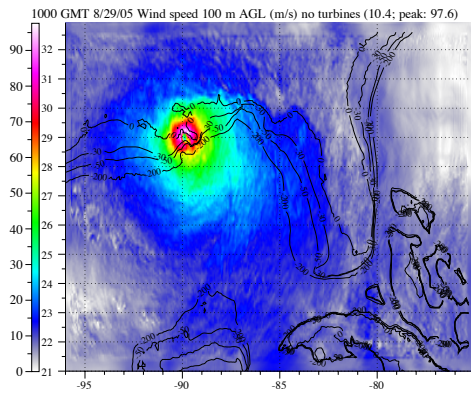
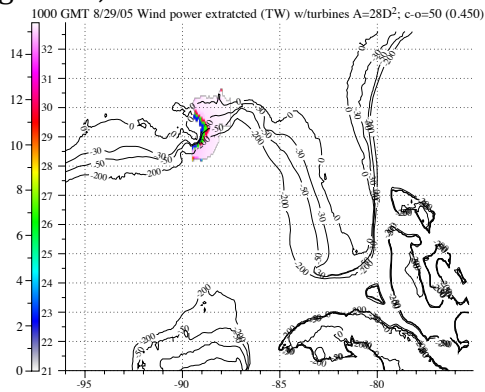


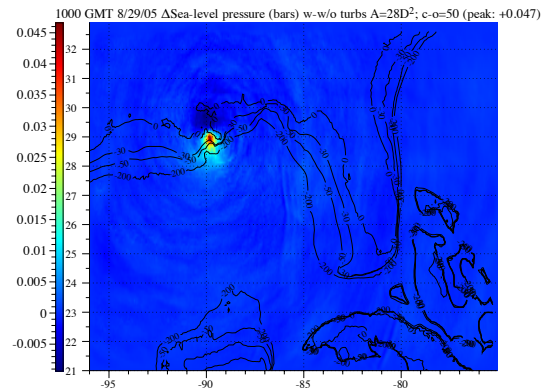
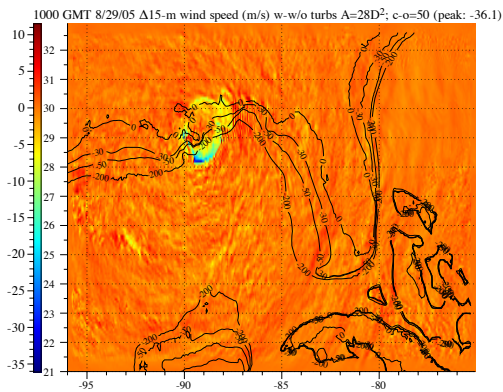
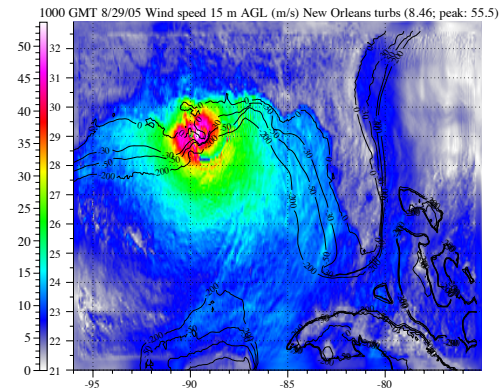
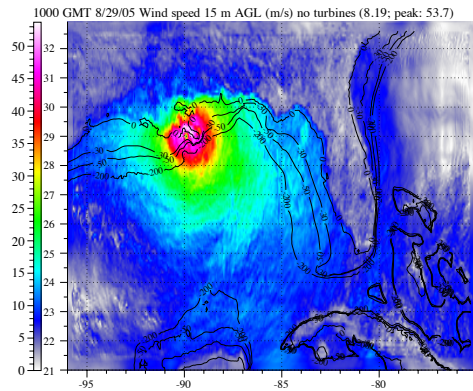
August 29, 2005, 06:00 GMT



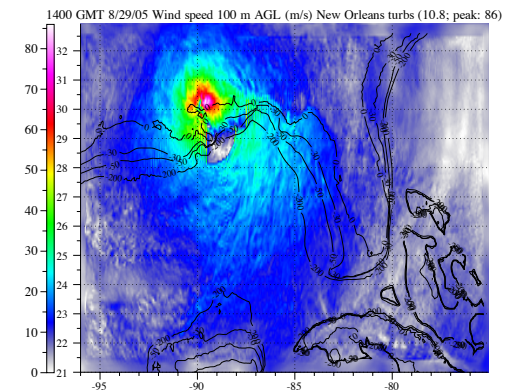
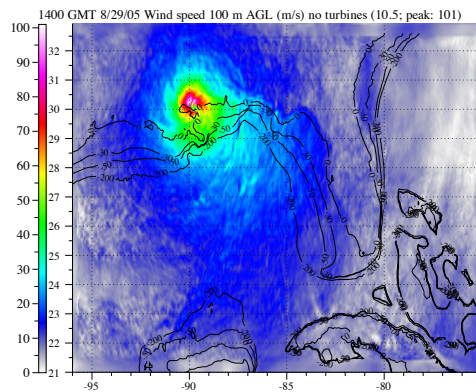
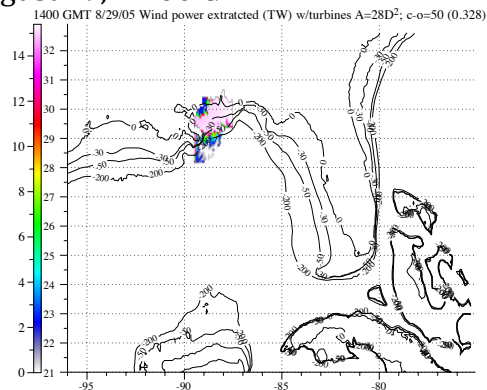


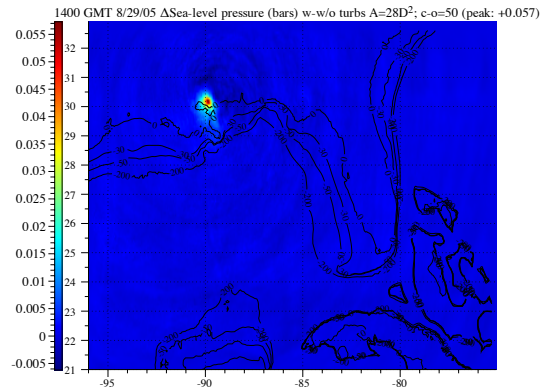
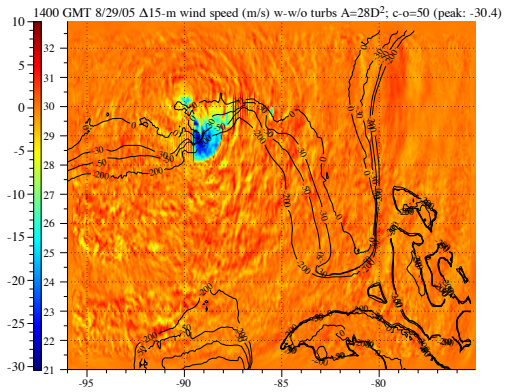
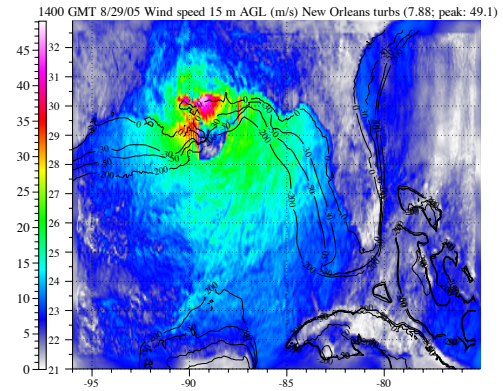
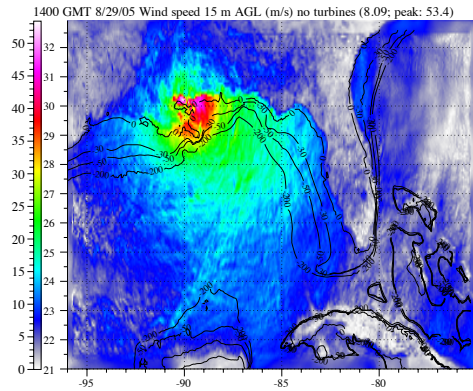
August 29, 10:00 GMT



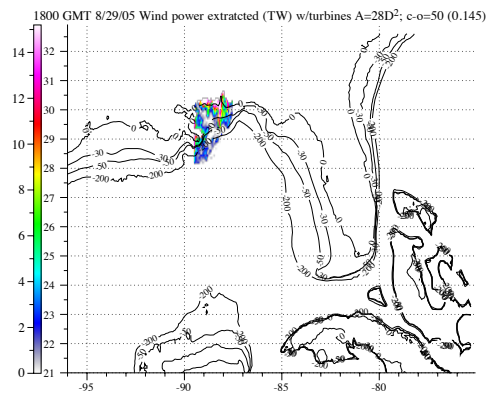


August 29, 14:00 GMT





August 29, 18:00 GMT



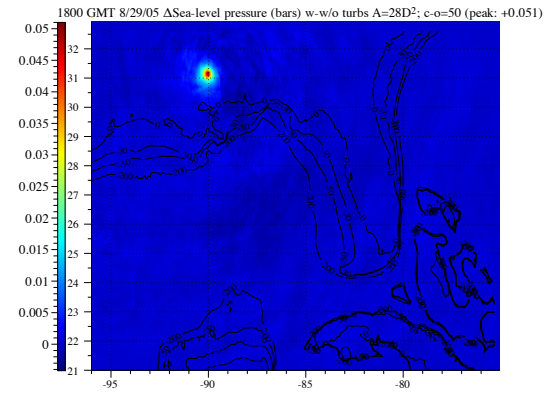
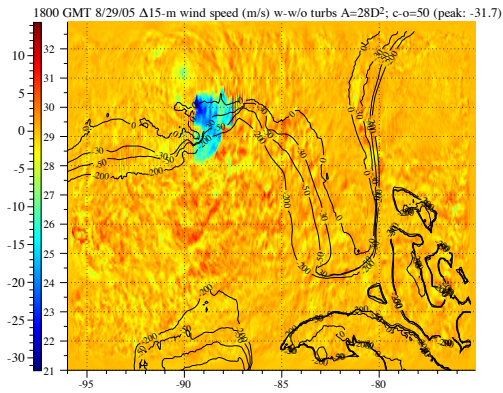
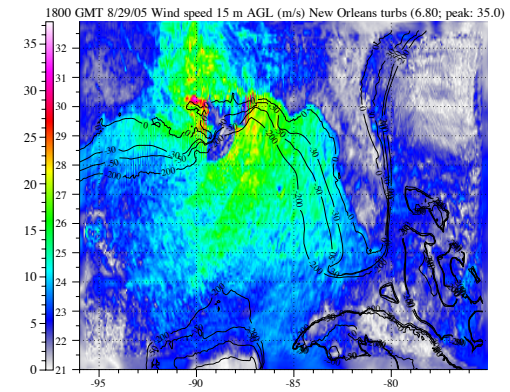
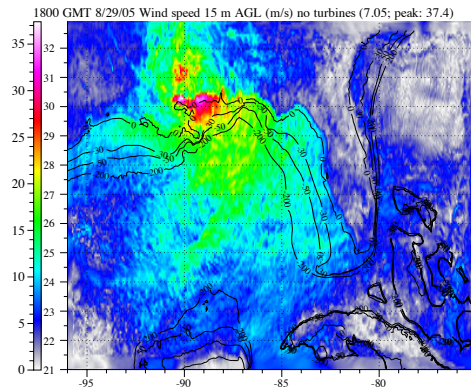
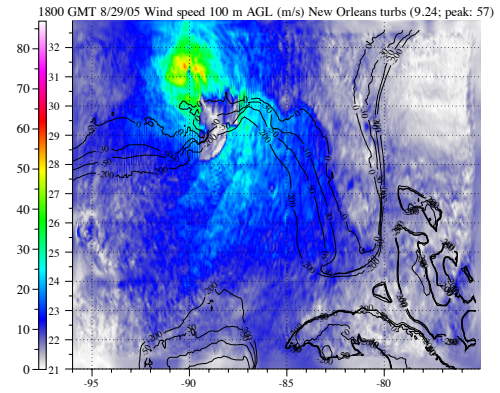
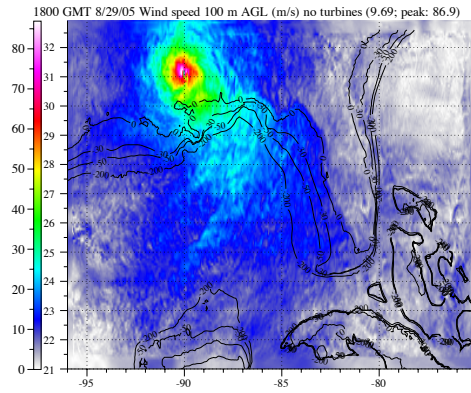
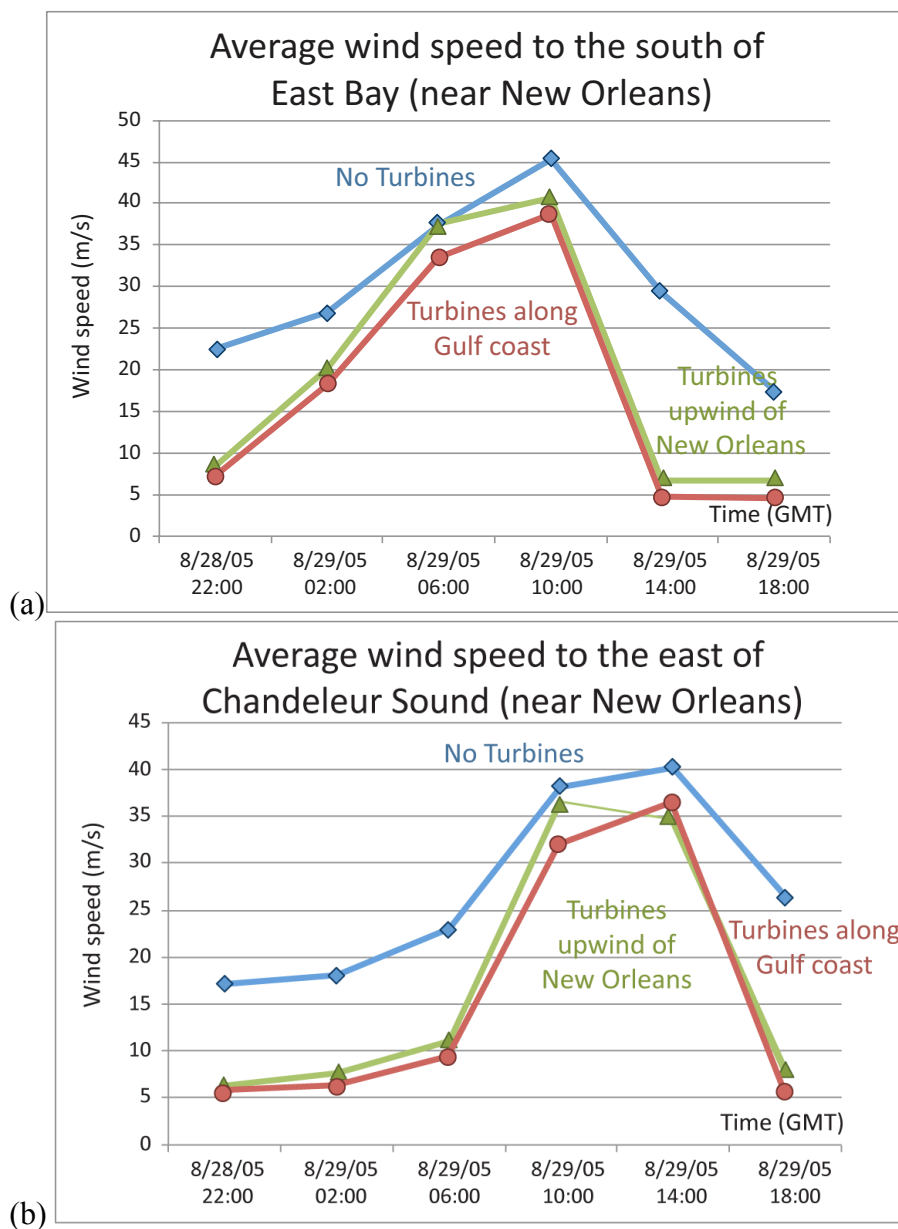


Figure S9. Time series of simulated wind speeds during Katrina averaged over: (a) area to the south of East Bay, near New Orleans (within the box 28.5N-29.0N and 89.5W-89.0W), with earliest landfall around 11 GMT on 8/29/05; (b) area to the east of Chandeleur Sound, near New Orleans (29.5N-30.0N and 89.5W-89.0W), with landfall around 14 GMT on 8/29; and (c) over the sector relevant for storm surge with winds directed towards the land, upwind of New Orleans, with variable coordinates ($t \leq 6$ GMT: 28.5N-30.5N and 89.5W-87W; $t = 10$ GMT: 29N-30.5N and 89.5W-87W; $t \geq 14$ GMT: 29.5N-30.5N and 89.5W-87W). The base case with no turbines has the highest wind speeds; reductions in wind speeds greater than 50% are found with turbines over the entire Gulf coast (Simulation A) and to the east of New Orleans (Simulation D), respectively, suggesting that wind turbines installed upwind of a populated region can reduce wind speed significantly in the region.



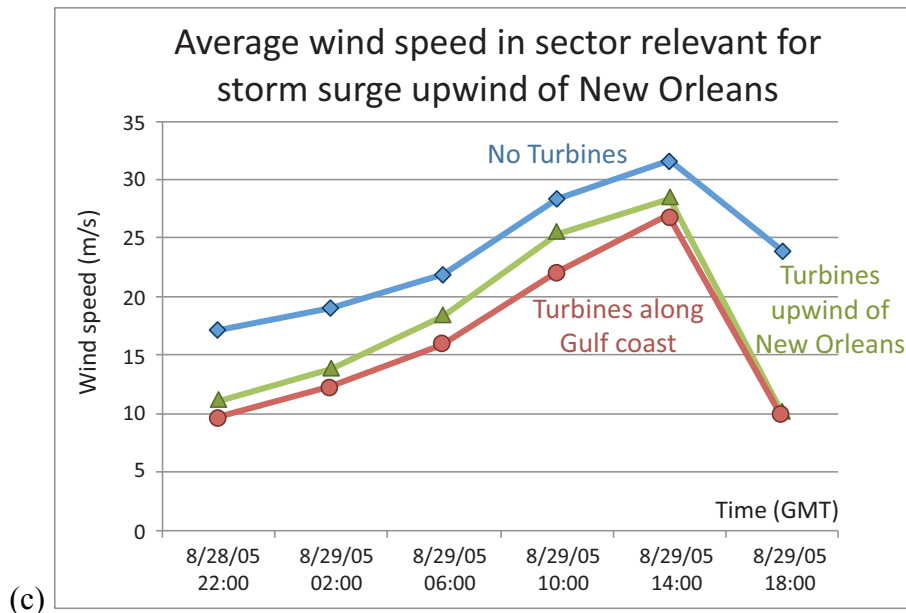
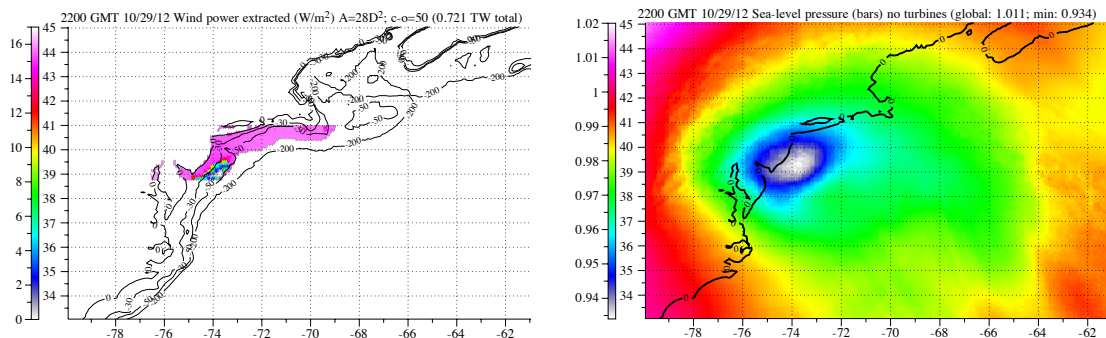
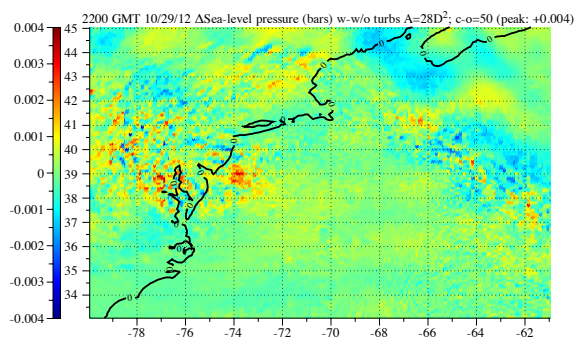
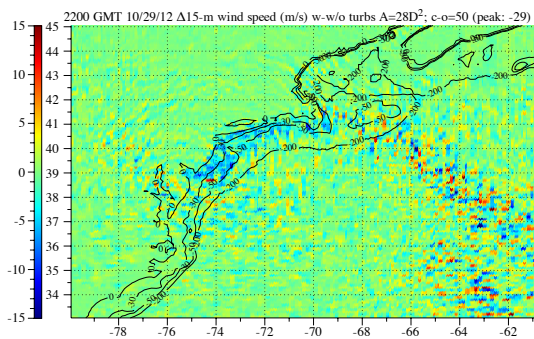
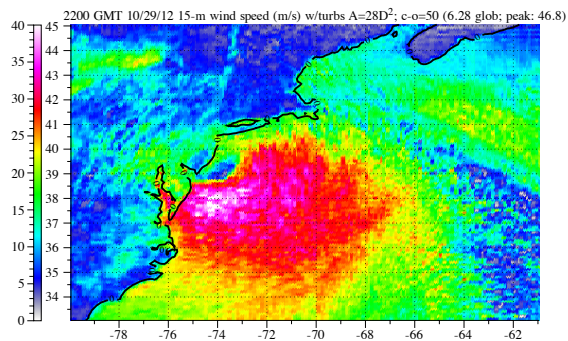
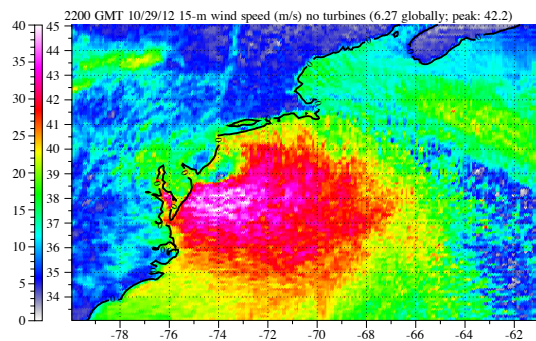


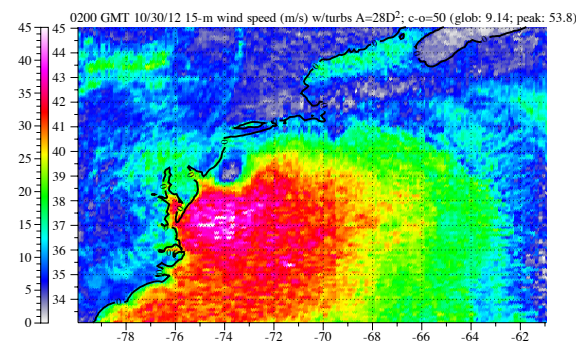
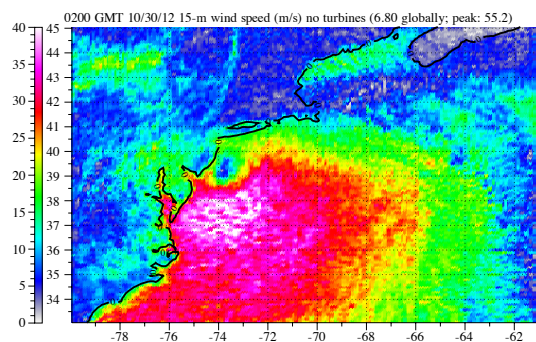
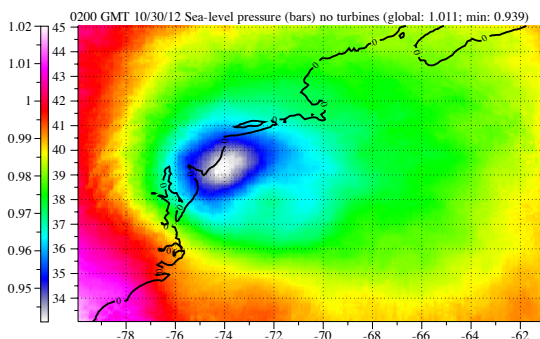
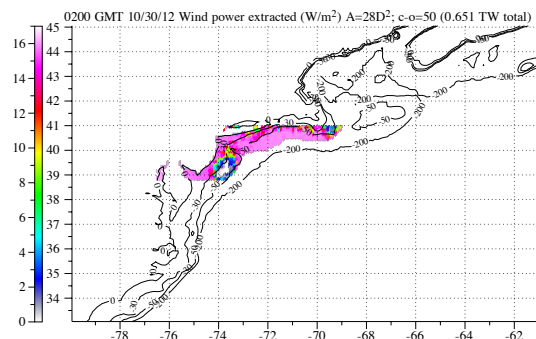
Figure S10. Time series of instantaneous power extraction (TW), sea-level pressure (bars), 15-m wind speeds (m/s) in the absence of wind turbines, 15-m wind speeds (m/s) in the presence of wind turbines, 15-m wind speed differences (m/s) with minus without turbines, and sea-level pressure differences (bars) with minus without turbines offshore of the east coast during Hurricane Sandy based on global-through-local stretched grid simulations (Simulation H in Table 1 of the main text). The turbines assumed were Enercon E-126 7.58-MW turbines with rotor diameter (D) of 127 m and hub height of 100 m. Spacing was 4-D x 7-D, and turbines were placed within 100 km of shore between Washington D.C. and New York City (Simulation H in Table 1 of the main text). The simulation was started at 18 GMT October 29, 2012, with the hurricane extant. The contours are bathymetry between 0-200 m depth.

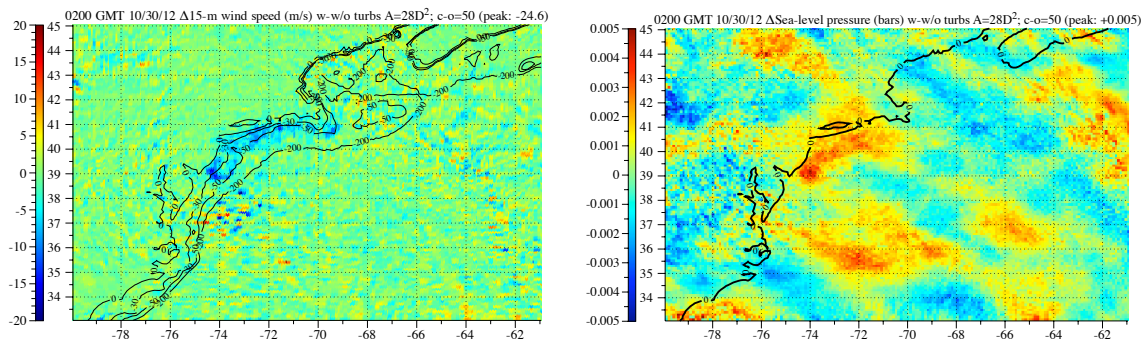
October 29, 22:00 GMT





October 30, 02:00 GMT





S4. Supporting References

- S1. Jacobson, M.Z. & Archer, C.L. Saturation wind power potential and its implications for wind energy. *Proc. Nat. Acad. Sci.* **109**, 15,679-15,684 (2012)
- S2. Jacobson, M.Z. GATOR-GCMM: A global through urban scale air pollution and weather forecast model. 1. Model design and treatment of subgrid soil, vegetation, roads, rooftops, water, sea ice, and snow. *J. Geophys. Res.* **106**, 5385-5402 (2001).
- S3. Jacobson, M.Z. Short-term effects of controlling fossil-fuel soot, biofuel soot and gases, and methane on climate, Arctic ice, and air pollution health. *J. Geophys. Res.* **115**, D14209 (2010).
- S4. Calaf, M., Parlange, M.B. & Meneveau, C. Large eddy simulation study of scalar transport in fully developed wind-turbine array boundary layers. *Phys. Fluids* **23**, 126603, doi:10.1063/1.3663376 (2011).
- S5. Barrie, D. B. & Kirk-Davidoff, D. B. Weather response to a large wind turbine array. *Atmos. Chem. Phys.* **10**, 769-775 (2010).
- S6. Arakawa, A. & Lamb, V.R. A potential enstrophy and energy conserving scheme for the shallow water equations. *Mon. Wea. Rev.* **109**, 18-36 (1981).
- S7. Walcek, C. J. & Aleksic, N. M. A simple but accurate mass conservative, peak-preserving, mixing ratio bounded advection algorithm with fortran code. *Atmos. Environ.* **32**, 3863-3880 (1998)
- S8. Jacobson, M.Z. & Ten Hoeve, J.E. Effects of urban surfaces and white roofs on global and regional climate. *J. Climate* **25**, 1028-1044 (2012).
- S9. Ketefian, G.S. & Jacobson, M.Z., A mass, energy, vorticity, and potential enstrophy conserving boundary treatment scheme for the shallow water equations. *J. Comp. Phys.* **228**, 1-32, doi:10.1016/j.jcp.2008.08.009 (2009).
- S10. Jacobson, M.Z. Studying ocean acidification with conservative, stable numerical schemes for nonequilibrium air-ocean exchange and ocean equilibrium chemistry. *J. Geophys. Res.* **110**, D07302, doi:10.1029/2004JD005220 (2005).
- S11. Garratt, J.R., The atmospheric boundary layer, Cambridge University Press, Cambridge, p. 101 (1992).
- S12. Jacobson, M.Z., Improvement of SMVGEAR II on vector and scalar machines through absolute error tolerance control. *Atmos. Environ.* **32**, 791-796 (1998).

- S13. Jacobson, M. Z. Analysis of aerosol interactions with numerical techniques for solving coagulation, nucleation, condensation, dissolution, and reversible chemistry among multiple size distributions. *J. Geophys. Res.* **107** (D19), 4366, doi:10.1029/2001JD002044 (2002).
- S14. Jacobson, M.Z., Kaufmann, Y.J. & Rudich, Y. Examining feedbacks of aerosols to urban climate with a model that treats 3-D clouds with aerosol inclusions, *J. Geophys. Res.*, **112**, D24205, doi:10.1029/2007JD008922 (2007).
- S15. Jacobson, M.Z. Investigating cloud absorption effects: Global absorption properties of black carbon, tar balls, and soil dust in clouds and aerosols. *J. Geophys. Res.* **117**, D06205, doi:10.1029/2011JD017218 (2012).
- S16. Jacobson, M.Z., Development of mixed-phase clouds from multiple aerosol size distributions and the effect of the clouds on aerosol removal. *J. Geophys. Res.* **108** (D8), 4245, doi:10.1029/2002JD002691 (2003).
- S17. Clarke, A.D., Owens, S.R. & Zhou J. An ultrafine sea-salt flux from breaking waves: Implications for cloud condensation nuclei in the remote marine atmosphere. *J. Geophys. Res.* **111**, D06202, doi:10.1029/2005JD006565 (2006).
- S18. Smith, M.H. & Harrison, N.M. The sea spray generation function. *J. Aerosol Sci.* **29**, Suppl. 1, S189-S190 (1998).
- S19. Jacobson, M.Z. & Streets, D.G. The influence of future anthropogenic emissions on climate, natural emissions, and air quality, *J. Geophys. Res.* **114**, D08118, doi:10.1029/2008JD011476 (2009).
- S20. Flanner, M.G. & Zender, C.S. Linking snowpack microphysics and albedo evolution. *J. Geophys. Res.* **111**, D12208, doi:10.1029/2005JD006834 (2006).
- S21. Toon, O.B., McKay, C.P., Ackerman, T.P. & Santhanam, K. Rapid calculation of radiative heating rates and photodissociation rates in inhomogeneous multiple scattering atmospheres. *J. Geophys. Res.* **94**, 16,287-16,301 (1989).
- S22. Jacobson, M.Z. A refined method of parameterizing absorption coefficients among multiple gases simultaneously from line-by-line data. *J. Atmos. Sci.*, **62**, 506-517 (2005).
- S23. Ackerman, T.P. & Toon, O.B. Absorption of visible radiation in atmosphere containing mixtures of absorbing and nonabsorbing particles. *Appl. Optics* **20**, 3661-3667 (1981).
- S24. Kirchstetter, T.W., Novakov, T. & Hobbs P.V. Evidence that spectral light absorption by aerosols emitted from biomass burning and motor vehicles is different due to organic carbon. *J. Geophys. Res.* **109**, D21208, doi:10.1029/2004JD004999 (2004).
- S25. Alexander, D.T.L., Crozier, P.A. & Anderson, J.R. Brown carbon spheres in East Asian outflow and their optical properties. *Science* **321**, 833-836, doi:10.1126/science.1155296 (2008).

- S26. Dunion, J.P. & Velden, C.S. The impact of the Saharan air layer on Atlantic tropical cyclone activity. *Bull. Amer. Meteor. Soc.* **85**, 353-365 (2004).
- S27. Zhang, H., McFarquhar, G.M., Saleeby, S.M. & Cotton, W.R. Impacts of Saharan dust as CCN on the evolution of an idealized tropical cyclone. *Geophys. Res. Lett.* **34**, L14812, doi: 10.1029/2007GL029 (2007).
- S28. Sun, D., Lau, K.M. & Kafatos, M., Contrasting the 2007 and 2005 hurricane seasons: Evidence of possible impacts of Saharan dry air and dust on tropical cyclone activity in the Atlantic basin. *Geophys. Res. Lett.* **35**, L15405, doi:10.1029/2008GL034529 (2008).
- S29. Chylek, P., Ramaswamy, V. & Cheng, R.J. Effect of graphitic carbon on the albedo of clouds. *J. Atmos. Sci.* **41**, 3076-3084 (1984).
- S30. Roy, S.B., Pacala, S.W. & Walko, R.L. Can large wind farms affect local meteorology. *J. Geophys. Res.* **109**, D19101, doi:10.1029/2004JD004763 (2004).
- S31. Masters, G.M. *Renewable and efficient electric power systems*. John Wiley & Sons, Hoboken, NJ (2004).
- S32. Mellor, G.L. & Yamada, T. Development of a turbulence closure model for geophysical fluid problems. *Revs. of Geophys. and Space Phys.* **20**, 851-875 (1982).
- S33. GFS (Global Forecast System), <http://nomads.ncdc.noaa.gov/data/gfs-avn-hi/> (2012), Accessed February 23, 2012.
- S34. Foster, R.C. Why rolls are prevalent in the hurricane boundary layer. *J. Atmos. Sci.*, **62**, 2647-2661 (2005).
- S35. Hoffman, R.N., Henderson, J.M., Leidner, S.M., Grassotti, C. & Nehr Korn, T. The Response of Damaging Winds of a Simulated Tropical Cyclone to Finite-Amplitude Perturbations of Different Variables. *J. Atmos. Sci.* **63**, 1924-1937 (2006).
- S36. Kempton, W., Archer, C.L., Dhanju, A., Garvine, R.W. & Jacobson, M.Z. Large CO₂ reductions via offshore wind power matched to inherent storage in energy end-uses. *Geophys. Res. Lett.* **34**, L02817 (2007).
- S37. Dvorak, M.J., Corcoran, B.A., Ten Hoeve J.E., McIntyre, N.J. & Jacobson, M.Z. U.S. East Coast offshore wind energy resources and their relationship to peak-time electricity demand. *Wind Energy*, doi:10.1002/we.1524, (2012).
- S38. Rose, S., Jaramillo, P., Small, M.J., Grossmann, I. & Apt, J. Quantifying the hurricane risk to offshore wind turbines. *Proc. Natl. Acad. Sci.* **109**, 3247-3252, (2011).
- S39. Powell, M.D. & Cocke, S. Hurricane wind fields needed to assess risk to offshore wind farms. *Proc Natl Acad Sci.*, **109**, E2192 (2012).
- S40. Rose, S., Jaramillo, P., Small, M.J., Grossmann, I., Apt, J. Reply to Powell and Cocke: On the probability of catastrophic damage to offshore wind farms from hurricanes in the U.S. Gulf Coast. *Proc. Natl. Acad. Sci.* **109**, E2193-E2194 (2012).
- S41. Kempton, W., Pimenta, F.M., Veron, D.E. & Colle, B.A. Electric power from offshore wind via synoptic-scale interconnection. *Proc. Natl. Acad. Sci.*, **107**, 7240-7245, (2010).

- S42. Budischak, C., Sewell, D., Thomson, H., Mach, L., Veron, D.E. & Kempton, W. Cost-minimized combinations of wind power, solar power, and electrochemical storage, powering the grid up to 99.9% of the time. *J. Power Sources* 225,, 60-74 (2013).
- S43. Emanuel, K. *Divine wind: the history and science of hurricanes*. Oxford University Press, 296 pp (2005).
- S44. Pugh, D. T. Tides, surges, and mean sea-level. John Wiley and Sons, 472 pp (1987).
- S45. Bowden, K. F. Physical oceanography of coastal waters. Ellis Horwood Limited, 302 pp (1983).
- S46. Reid, R. O. Tides and storm surges. In Handbook of coastal and ocean engineering, Volume 1, Wave phenomena and coastal structures, Ed. J. B. Herbich, Gulf Publishing Company, 533-590 (1999).
- S47. Irish, J.L., Resio, D.T. & Ratcliff, J.J. The influence of storm size on hurricane surge. *J Phys. Oceanog.* **38**, 2003-2013 (2008).
- S48. Conner, W. C., Kraft, R. H. & Harris, D. L. Empirical methods for forecasting the maximum storm tide due to hurricanes and other tropical storms. *Monthly Weather Review* **85**, 113-116 (1957).
- S49. Russo, E. P. Estimating hurricane storm surge amplitudes for the Gulf of Mexico and Atlantic coastlines of the United States. *OCEANS '98 Conference Proceedings* **3**, 1301-1305. doi: 10.1109/OCEANS.1998.726278 (1998).
- S50. Young, I. R., A parametric hurricane wave prediction model. *Proceedings of the International Twenty-first Coastal Engineering Conference*, Malaga, Spain, pp. 1098-1112 (1988).
- S51. National Hurricane Center, Sea, Lake, and Overland Surges from Hurricanes (SLOSH) model, http://www.nhc.noaa.gov/ssurge/ssurge_slosh.shtml, (2012), Accessed January 13, 2013.
- S52. Jonkman, S.N., Bockarjova, M., Kok, M. & Bernardini, P. Integrated hydrodynamic and economic modelling of flood damage in the Netherlands. *Ecological Economics* 66: 77-90 (2008).
- S53. Unanwa, C.O., McDonald, J.R., Mehta, K.C. & Smith. D.A. The development of wind damage bands for buildings. *J. Wind Eng. Industrial Aerodynamics* **84**, 119-149 (2000).
- S54. McAdie, C.J., Landsea, C.W., Neumann, C.J., David, J.E. & Blake, E.S., Tropical Cyclones of the North Atlantic Ocean 1851-2006 *Technical Report HCS 6-2*, National Oceanic and Atmospheric Administration, http://www.nhc.noaa.gov/pdf/TC_Book_Atl_1851-2006_lowres.pdf, (2009), Accessed August 4, 2013.
- S55. Levitt, A.C., Kempton, W., Smith, A.P., Musial, W., Firestone, J. Pricing offshore wind power. *Energy Policy* **39**, 6408-6421 (2011).
- S56. IOC, IHO, BODC (2003), Centenary edition of the GEBCO digital Atlas published on CD-ROM on behalf of the intergovernmental oceanographic commission and the international hydrographic organization as part of the general bathymetric chart of

the oceans. British Oceanographic Data Centre, Liverpool,
http://www.bodc.ac.uk/data/online_delivery/gebco/, Accessed January 13, 2013
(2003).